Feedback-induced desynchronization and oscillation quenching in a population of globally coupled oscillators

Ayumi Ozawa [*] and Hiroshi Kori

Department of Complexity Science and Engineering, The University of Tokyo, Chiba 277-8561, Japan

(Received 8 February 2021; accepted 20 May 2021; published 28 June 2021)

Motivated from a wide range of applications, various methods to control synchronization in coupled oscillators have been proposed. Previous studies have demonstrated that global feedback typically induces three macroscopic behaviors: synchronization, desynchronization, and oscillation quenching. However, analyzing all of these transitions within a single theoretical framework is difficult, and thus the feedback effect is only partially understood in each framework. Herein, we analyze a model of globally coupled phase oscillators exposed to global feedback, which shows all of the typical macroscopic dynamical states. Analytical tractability of the model enables us to obtain detailed phase diagrams where transitions and bistabilities between different macroscopic states are identified. Additionally, we propose strategies to steer the oscillators into targeted states with minimal feedback strength. Our study provides a useful overview of the effect of global feedback and is expected to serve as a benchmark when more sophisticated feedback needs to be designed.

DOI: 10.1103/PhysRevE.103.062217

I. INTRODUCTION

Synchronization is a self-organization phenomenon that occurs in interacting oscillatory elements and is widely observed [1–5]. The resultant coherent oscillation is desirable in some systems. For example, synchronization is essential for the normal functioning of power grids [6]. Other beneficial effects of synchronization include the enhanced precision in biological oscillatory systems [4,7–10], coordinated locomotion of animals and robots [11], and reduced congestion in models of traffic flow [12,13].

However, synchronization may also cause problems. At the Millennium Footbridge in London, the steps of the pedestrians were synchronized, and considerable lateral movement of the bridge was observed [14]. Synchronization is also associated with neurological disorders. The local field potentials recorded from the brains of Parkinsonian patients and model animals often display marked oscillations, which are considered to be reflections of coherent neuronal activities [15]. Although the mechanism of Parkinson's disease is not well understood yet, exaggerated synchronization is one of the possible factors that induces related symptoms [16]. For some types of Parkinsonian patients, deep brain stimulation (DBS), which involves electrical stimulation to particular regions of the brain, may suppress the pathological collective oscillation and motor symptoms [15,17]. However, this treatment is sometimes accompanied by negative side effects [18,19]. Thus, milder ways of stimulation need to be developed.

The wide range of desirable and undesirable synchronization phenomena has drawn substantial research attention to the control of synchronization. As a control implementation, global feedback loops are known to be effective. In [20], the authors experimentally demonstrated that a synchronously oscillating state can be stabilized in a surface chemical reaction that inherently exhibits turbulent oscillatory dynamics. Global feedback may also desynchronize oscillator assemblies. Several types of mean-field feedback that efficiently desynchronize oscillators have been proposed [21–29]. Moreover, other behaviors may be realized through global feedback. It is proved that in a particular class of phase oscillators, the oscillation death state, in which the mean-field oscillation terminates, can be stabilized via global mean-field feedback [27]. Oscillation death is known to appear in various coupled oscillator systems [30].

These extensive studies [20–29] elucidated that global feedback typically stabilizes the synchronous, asynchronous, or oscillation-death states. However, in the oscillator models and feedback forms considered thus far, analytically treating all of these macroscopic states is difficult, and hence, a comprehensive phase diagram has not been obtained. With only partial knowledge being available on the phase diagram, feedback control may fail to realize a desired state owing to the unexpected stabilization of other states. Detailed phase diagrams of an analytically tractable model would provide an insight into a general principle of feedback control and help design and tune the feedback scheme.

Herein, we consider the Sakaguchi-Kuramoto model, which describes a population of nonidentical phase oscillators with global coupling, as a coupled-oscillator model and incorporate a global mean-field feedback loop into the system.

We show that the system exhibits all three typical macroscopic states: the asynchronously oscillating state, the synchronously oscillating state, and the oscillation-death state. By invoking the Ott-Antonsen ansatz [31,32], we comprehensively perform the existence and stability analysis of the macroscopic states, thus obtaining detailed phase diagrams in the space of feedback parameters for different coupling

[*] ozawa-ayumi@g.ecc.u-tokyo.ac.jp

strengths. Our analysis elucidates (1) the dependency of the feedback effect on the parameters of the oscillator model; (2) the optimal feedback parameters for stabilizing the asynchronous state with minimal feedback strength; and (3) the existence of the bistability between the oscillation-death state and one of the other two states. The obtained phase diagrams are numerically validated. In addition, we propose a strategy for realizing the asynchronous state in the bistable region. Finally, to support the robustness of our results, we numerically investigate another model that belongs to a more general class of oscillator models.

II. MODEL

We consider globally coupled phase oscillators under global feedback, given as

$$\frac{d\theta_i}{d\tilde{t}} = \tilde{\omega}_i + \frac{\tilde{K}}{N}\sum_{j=1}^{N}\sin(\theta_j - \theta_i + \beta) + \tilde{E}\sin(\theta_i + \alpha)F(\boldsymbol{\theta}), \tag{1}$$

where $\theta_i(\tilde{t})$ and $\tilde{\omega}_i$ $(i = 1, \ldots, N)$ represent the phase and natural frequency of the ith oscillator, respectively; $\tilde{K} \geqslant 0$ and $\tilde{E} \geqslant 0$ represent the strength of coupling and feedback, respectively; and α and β are parameters, which are usually nonvanishing in real oscillator systems [33,34]. The function $F(\boldsymbol{\theta}) = F(\theta_1, \ldots, \theta_N)$ describes a global feedback and $\sin(\theta_i + \alpha)$ is the phase sensitivity to the feedback. In particular, we consider

$$F(\boldsymbol{\theta}) = \frac{1}{N}\sum_{j=1}^{N}\cos(\theta_j - \delta), \tag{2}$$

$$= R\cos(\Theta - \delta), \tag{3}$$

where δ is a parameter referred to as the phase offset in the feedback, and $R = R(t)$ $(0 \leqslant R \leqslant 1)$ and $\Theta = \Theta(t)$ $(0 \leqslant \Theta < 2\pi)$ are the order parameter and mean phase defined by

$$r := Re^{i\Theta} = \frac{1}{N}\sum_{j=1}^{N}e^{i\theta_j}. \tag{4}$$

The R value indicates the synchronization level. The complex valued function $r = r(t)$ is referred to as the complex order parameter. Equation (1) reduces to the Kuramoto-Sakaguchi model [35] in the absence of feedback, i.e., for $\tilde{E} = 0$. See Appendix A for the derivation of Eq. (1) from a general class of coupled limit-cycle oscillators. As discussed in Appendix A, $F(\boldsymbol{\theta})$ corresponds to a linear function of mean fields in the limit-cycle model introduced in Appendix A, and the parameters $\tilde{E}$ and δ can be tuned to arbitrary values when two output signals are observed from individual oscillators. Alternatively, it can be implemented when $R(t)$ and $\Theta(t)$ are inferred online.

For analytical tractability, we assume $\tilde{\omega}_i$ to be drawn from the Lorentzian distribution $\tilde{g}(\tilde{\omega}) = \frac{\tilde{\gamma}}{\pi}\frac{1}{(\tilde{\omega}-\omega_0)^2+\tilde{\gamma}^2}$, where $\tilde{\gamma} > 0$ and $\omega_0 > 0$. Without loss of generality, we decrease the number of parameters by introducing nondimensional quantities $t = \omega_0\tilde{t}$, $\gamma = \frac{\tilde{\gamma}}{\omega_0}$, $K = \frac{\tilde{K}}{\omega_0}$, $E = \frac{\tilde{E}}{\omega_0}$, and further replacing $\theta_i + \alpha$ by θ_i for $i = 1, \ldots, N$ and $\delta + \alpha$ by δ. The resultant equation is

$$\frac{d\theta_i}{dt} = \omega_i + \frac{K}{N}\sum_{j=1}^{N}\sin(\theta_j - \theta_i + \beta) + E\sin\theta_i F(\boldsymbol{\theta}), \tag{5}$$

or

$$\dot{\theta}_i = \omega_i + KR\sin(\Theta - \theta_i + \beta) + ER\cos(\Theta - \delta)\sin\theta_i, \tag{6}$$

where ω_i is drawn from

$$g(\omega) = \frac{\gamma}{\pi}\frac{1}{(\omega - 1)^2 + \gamma^2}. \tag{7}$$

Now the mean frequency is set to unity. Equation (6) with Eqs. (2) and (7) is analyzed below. There are six parameters involved: $N, K > 0, E > 0, \beta, \delta$, and γ.

It is known that for $N \to \infty$, a certain class of oscillator assemblies including Eq. (6) has a low-dimensional manifold, on which a reduced dynamical equation can be obtained [31,32]. By following [36], we obtain a closed equation for r on the manifold, given as

$$\dot{r} = \left(-\gamma + \frac{Ke^{i\beta}}{2} + i\right)r - \frac{Ke^{-i\beta}}{2}|r|^2 r - \frac{ER\cos(\Theta - \delta)}{2}(1 - r^2). \tag{8}$$

Here we redefined $r = Re^{i\Theta}$ as its continuous analog

$$r = \iint \rho(\theta,\ \omega,\ t)e^{i\theta}d\theta\, d\omega, \tag{9}$$

where $\rho(\theta, \omega, t)d\theta\, d\omega$ is the fraction of the oscillators with natural frequencies between ω and $\omega + d\omega$ and phases between θ and $\theta + d\theta$ at time t. For finite but sufficiently large N, Eq. (8) is expected to appropriately approximate the behavior of $r(t)$ in Eq. (6) after a transient time.

Henceforth, we assume $|\beta| < \pi/2$; the coupling promotes synchronization.

III. EFFECT OF FEEDBACK ON THE MACROSCOPIC STATE

A. Classification of macroscopic states

Dynamical properties of the system described by Eq. (8) in the absence of feedback ($E = 0$) are evident. This system always has a global attractor for any parameter values within $K \geqslant 0$ and $-\frac{\pi}{2} < \beta < \frac{\pi}{2}$. There are two global attractors: the steady solution $r(t) = 0$ for $K \leqslant K_c$ and the limit-cycle solution $r(t) = r_0 e^{i\tilde{\Omega}t}$ for $K > K_c$, where $K_c = 2\gamma/\cos\beta$, $r_0 = [1 - K_c/K]^{1/2}$, and $\tilde{\Omega} = 1 + K\sin\beta - \gamma\tan\beta$. The former corresponds to the asynchronous state, where the oscillators rotate with their natural frequencies. The latter corresponds to the synchronously oscillating state, where a subpopulation of the oscillators is phase locked to the oscillating mean field. Figures 1(a)–1(c) show typical dynamics of Eq. (6) for $E = 0$.

In addition to these two attractors, a stable steady solution $r(t) = r^* \neq 0$ may arise in the presence of the feedback ($E > 0$). We refer to the macroscopic state corresponding to this solution as the oscillation-death state because of the cessation of the microscopic and macroscopic oscillations explained below. To understand the dynamics of individual oscillators in

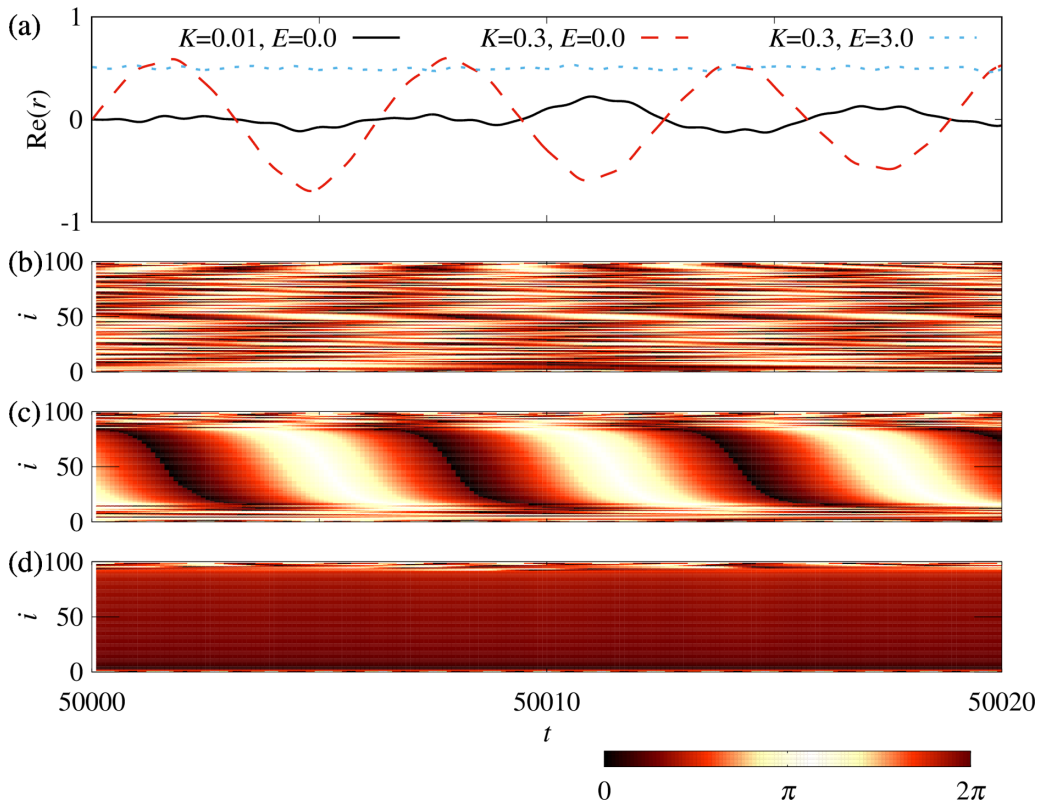

FIG. 1. Three types of macroscopic state of the $N = 100$ oscillators described by Eq. (6). (a) Time series of the real part of the complex order parameter r for different parameter regimes. The black solid, red dashed, and blue dotted lines represent the solutions corresponding to the asynchronously oscillating state, the synchronously oscillating state, and the oscillation-death state, respectively. The coupling strength and feedback parameters are set to $K = 0.01$ and $E = \delta = 0$ (solid black line), $K = 0.3$ and $E = \delta = 0$ (red dashed line), and $K = 0.3$, $E = 3.0$, and $\delta = -\pi/3$ (blue dotted line). The other parameters are $\gamma = 0.1$ and $\beta = 0$. (b)–(d) Time series of the individual oscillators. The vertical axis is the index of the oscillator, and the color scale represents its phase. The natural frequency ω_i is set to be monotonically increasing with the oscillator index i: $\omega_i = 1 + \gamma \tan[\frac{i\pi}{N} - \frac{(N+1)\pi}{2N}]$. The parameters for (b), (c), and (d) are identical to those of the black solid, red dashed, and blue dotted lines in Fig. 1(a), respectively.

the oscillation-death state ($r(t) = r^*$), let us consider Eq. (6). Inserting $r^* = R^* e^{i\Theta^*}$ into Eq. (6), we obtain

$$\dot{\theta}_i = \omega_i + A \sin(\theta_i + B), \tag{10}$$

where

$$A = R^*\{[E\cos(\Theta^* - \delta) - K\cos(\Theta^* + \beta)]^2 + [K\sin(\Theta^* + \beta)]^2\}^{1/2}, \tag{11}$$

$$\tan B = \frac{K\sin(\Theta^* + \beta)}{E\cos(\Theta^* - \delta) - K\cos(\Theta^* + \beta)}. \tag{12}$$

A stable fixed point of Eq. (10) exists for $|\omega_i| < |A|$, which implies that the oscillators with $|\omega_i| < |A|$ cease their oscillations. Thus, the solution $r(t) = r^* \neq 0$ corresponds to the oscillation-death state, where a subpopulation of the oscillators and the mean field quit oscillations. Figure 1(d) and the blue dotted line in Fig. 1(a) exemplify the dynamics of the oscillators and the order parameter, respectively, in the oscillation-death state.

B. Bifurcation analysis and phase diagrams

The following bifurcation analysis of Eq. (8) enables us to obtain the phase diagrams shown in Fig. 2.

First, we analyze the bifurcation of the fixed point $r = 0$, the asynchronous state. Substituting $r = x + iy$ ($x,\ y \in \mathbb{R}$) into Eq. (8) and linearizing the equations for dx/dt and dy/dt around $(x, y) = (0, 0)$, we obtain the stability matrix

$$L = \begin{bmatrix} \Lambda - \frac{E}{2}\cos\delta & -\Omega - \frac{E}{2}\sin\delta \\ \Omega & \Lambda \end{bmatrix}, \tag{13}$$

where $\Lambda = -\gamma + \frac{K}{2}\cos\beta$ and $\Omega = 1 + \frac{K}{2}\sin\beta$. The quantity Ω represents the frequency of collective oscillation at its onset, at $K = K_c$, in the absence of feedback.

The saddle-node (SN), transcritical, pitchfork, and Hopf bifurcations are the codimension-one bifurcations that alter the local stability and/or number of fixed points. The first three bifurcations occur when one of the eigenvalues of the stability matrix vanishes, which can be captured by its necessary condition $|L| = 0$. Hopf bifurcation occurs when both eigenvalues of L become purely imaginary, $\mathrm{Tr}L = 0$ and $|L| > 0$.

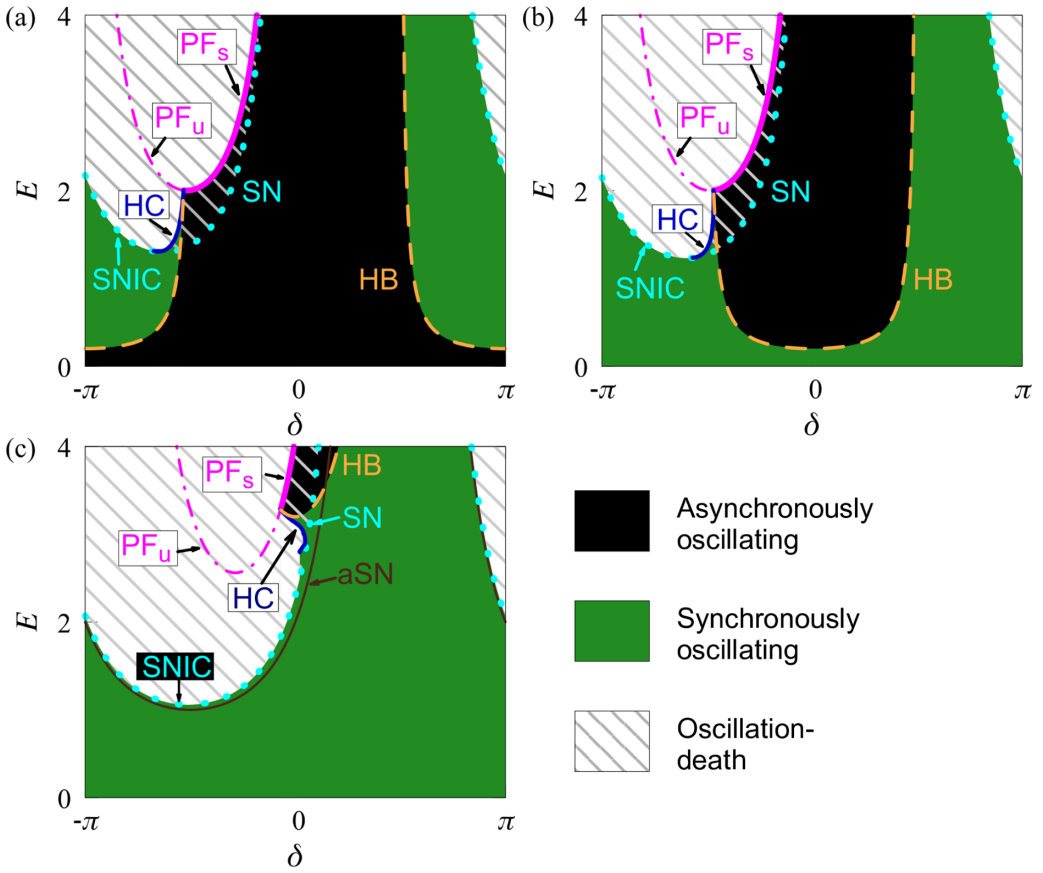

FIG. 2. Phase diagrams of the macroscopic state based on the stable solutions of Eq. (8) for (a) $K = 0.1 < K_c$, (b) $K = 0.3 > K_c$, and (c) $K = 1.8 \gg K_c$, where $K_c = 2\gamma/\cos\beta = 0.2$. Other parameters are $\gamma = 0.1$ and $\beta = 0$. The black, green, and shaded regions correspond to the asynchronous, synchronously oscillating, and oscillation-death states, respectively. The curves labeled as HB, SN, SNIC, and HC represent the Hopf bifurcation of the origin, the saddle-node bifurcation involving nonzero fixed points, the saddle-node bifurcation on an invariant circle, and the heteroclinic bifurcation, respectively. The curve labeled as PFs corresponds to the pitchfork bifurcation involving the stable fixed point at the origin, while the one labeled as PFu corresponds to the pitchfork bifurcation involving only unstable fixed points. In Fig. 2(c) the approximate SN (aSN) curve defined as $E = E_{\rm lower}$, where $E_{\rm lower}$ is given by Eq. (24), is also illustrated.

Solving $\mathrm{Tr}L = 0$ for E under the condition $|L| > 0$ yields the Hopf bifurcation (HB) curve

$$E_{\rm hopf} = \frac{4\Lambda}{\cos\delta}, \tag{14}$$

where δ satisfies

$$-\Lambda^2 + \Omega^2 + 2\Lambda\Omega\tan\delta > 0. \tag{15}$$

The curve defined by Eqs. (14) and (15) is depicted by the orange dashed line in Figs. 2(a)–2(c). Because $\mathrm{Tr}L = 2\Lambda(1 - E/E_{\rm hopf})$, the asynchronous state is unstable for $E < E_{\rm hopf}$ (resp. $E > E_{\rm hopf}$) when $\Lambda > 0$ (resp. $\Lambda < 0$). The bifurcation is revealed to be supercritical by the weakly nonlinear analysis performed in Appendix C. Therefore, a continuous transition between the asynchronous and synchronous states occurs on this curve.

The condition $|L| = 0$ yields another bifurcation curve:

$$E_{\rm pf} = \frac{2(\Lambda^2 + \Omega^2)}{\Lambda\cos\delta - \Omega\sin\delta}. \tag{16}$$

On this curve, the pitchfork bifurcation occurs because Eq. (8) is invariant under the change of $r \to -r$. See Appendix B for the transformation of Eq. (8) to a normal form and for a brief explanation of why this bifurcation cannot be a transcritical or SN bifurcation. Because $|L|$ can be described as $|L| = (\Lambda^2 + \Omega^2)(1 - E/E_{\rm pf})$, the asynchronous state is unstable for $E > E_{\rm pf}$ when $\Lambda\Omega \neq 0$. The stability of a fixed point changes through this bifurcation if the nonzero eigenvalue of the stability matrix is negative, i.e., $\mathrm{Tr}L < 0$, or

$$2\Lambda < \frac{\Lambda^2 + \Omega^2}{\Lambda - \Omega\tan\delta}. \tag{17}$$

The curve defined by Eqs. (16) and (17) is highlighted using a magenta solid line labeled as PFs in Fig. 2. On this bifurcation curve, the asynchronous state loses its stability. Moreover, weakly nonlinear analysis performed in Appendix B implies that this bifurcation is subcritical in the parameter region considered in Fig. 2.

This suggests the existence of the bistability between the asynchronous and oscillation-death states near the curve, which will be numerically confirmed in Sec. III C.

The pitchfork bifurcation occurs to an unstable fixed point if the nonzero eigenvalue of the stability matrix on the bifurcation curve is positive, $\mathrm{Tr}L > 0$. We thus obtain the curve for this bifurcation, which is defined by Eqs. (16) and (17) but with the opposite inequality. The obtained curve is shown by

the dot-dashed line labeled as PFu in Fig. 2. Because no stable state emerges with this bifurcation, the curve is not relevant to the phase diagram.

Next, we investigate the bifurcation of the fixed point $r^* \neq 0$, the oscillation-death state. For convenience, we express Eq. (8) using polar coordinates:

$$\frac{dR}{dt} = R\left(-\gamma + (1-R^2)\left\{ \frac{K}{2}\cos\beta - \frac{E}{4}[\cos(\delta - 2\Theta) + \cos\delta] \right\} \right), \tag{18a}$$

$$\frac{d\Theta}{dt} = 1 + (1+R^2)\left\{ \frac{K}{2}\sin\beta + \frac{E}{4}[\sin\delta - \sin(\delta - 2\Theta)] \right\}. \tag{18b}$$

A fixed point $r^* = R^* e^{i\Theta^*}$ is given as a solution to $dR/dt = 0$ and $d\Theta/dt = 0$; however, this is difficult to solve explicitly. Nevertheless, we can still obtain the stability matrix by linearizing Eq. (18) around $(R, \Theta) = (R^*, \Theta^*)$, as

$$M = \begin{bmatrix} -\frac{2R^{*2}\gamma}{1-R^{*2}} & -\frac{E}{2}R^*(1-R^{*2})\sin(\delta - 2\Theta^*) \\ -\frac{2R^*}{R^{*2}+1} & \frac{E}{2}(R^{*2}+1)\cos(\delta - 2\Theta^*) \end{bmatrix}. \tag{19}$$

Below we show that the bifurcation curve can be obtained as a function of R^* and drawn in the phase diagram by varying R^* in the range of $0 < R^* < 1$.

By solving $|M| = 0$ and using the identity $\sin^2(\delta - 2\Theta^*) + \cos^2(\delta - 2\Theta^*) = 1$, we obtain

$$\sin(\delta - 2\Theta^*) = \pm\frac{1}{\sqrt{1+\xi^2}}, \tag{20a}$$

$$\cos(\delta - 2\Theta^*) = \mp\frac{\xi}{\sqrt{1+\xi^2}}, \tag{20b}$$

where

$$\xi = \frac{(R^{*2}-1)^2}{\gamma(R^{*2}+1)^2}. \tag{21}$$

By substituting Eq. (20) into Eq. (18) and inserting $dR/dt = d\Theta/dt = 0$, we obtain

$$E = \pm\frac{\sqrt{\xi^2+1}[(2\gamma + KQ_-\cos\beta)^2 + \gamma\xi(KQ_+\sin\beta + 2)^2]}{\xi(4\gamma - KQ_-{}^2\cos\beta + \gamma KQ_+{}^2\sin\beta)}, \tag{22a}$$

$$\cos\delta = \pm\frac{2\xi(2\gamma + KQ_-\cos\beta)(4\gamma - KQ_-{}^2\cos\beta + \gamma KQ_+{}^2\sin\beta)}{\sqrt{\xi^2+1}Q_-[(2\gamma + KQ_-\cos\beta)^2 + \gamma\xi(KQ_+\sin\beta + 2)^2]} \pm \frac{\xi}{\sqrt{\xi^2+1}}, \tag{22b}$$

$$\sin\delta = \mp\frac{2\xi(KQ_+\sin\beta + 2)(4\gamma - KQ_-{}^2\cos\beta + \gamma KQ_+{}^2\sin\beta)}{\sqrt{\xi^2+1}Q_+[(2\gamma + KQ_-\cos\beta)^2 + \gamma\xi(KQ_+\sin\beta + 2)^2]} \pm \frac{1}{\sqrt{\xi^2+1}}, \tag{22c}$$

where $Q_+ = 1 + R^{*2}$ and $Q_- = -1 + R^{*2}$. Inserting $0 < R^* < 1$ into Eq. (22) yields the cyan dotted curve in Fig. 2. As rationalized below, this curve represents the SN bifurcation at which stable and unstable oscillation death solutions that exist in the area surrounded by the curve collide and disappear. If transcritical or pitchfork bifurcation occurred on the curve, there should be a fixed point $r^* \neq 0$ below the curve. Such a fixed point may not disappear unless a bifurcation involving that point occurs, thus it should persist up to the parameter region of $E = 0$. However, this contradicts the fact that no isolated fixed point except $r = 0$ exists at $E = 0$. Thus, a SN bifurcation occurs on the curve. We now know that a pair of fixed points arises through the bifurcation, but their stability remains unclear. Expressing $\mathrm{Tr}M$ as a function of R^*, we numerically confirmed that $\mathrm{Tr}M < 0$ holds on the bifurcation curve. This implies that a stable node and a saddle collide on the bifurcation curve. Therefore, we conclude that a stable oscillation-death state exists inside the curve and disappears on the curve.

It is useful to obtain an approximate expression for the SN bifurcation as a function of δ. To this end, for some parameter regions, we derive a necessary condition and a sufficient condition for a nonzero fixed point (R^*, Θ^*) to exist. If a nonzero fixed point (R^*, Θ^*) exists, it must satisfy $d\Theta/dt|_{\Theta=\Theta^*} = 0$, or

$$E = \frac{4 + 2K(1+R^{*2})\sin\beta}{(1+R^{*2})[\sin(\delta - 2\Theta^*) - \sin\delta]}. \tag{23}$$

The numerator on the right-hand side is positive when $\Omega' := 1 + K\sin\beta > 0$. In this case, a lower bound $E_{\mathrm{lower}} \leqslant E$ is given by Eq. (23) with $R^{*2} = 1$ and $\sin(\delta - 2\Theta^*) = 1$:

$$E_{\mathrm{lower}} = \frac{2\Omega'}{1 - \sin\delta}. \tag{24}$$

Thus, when $\Omega' > 0$, a necessary condition for the existence of a nonzero fixed point is given by

$$E \geqslant E_{\mathrm{lower}}. \tag{25}$$

Next, we address a sufficient condition for the existence of a nonzero fixed point. We restrict ourselves to the parameter region where $\Omega' > 0$ and $K > 2K_c$ holds. Then, for the parameter region under consideration, as shown in Appendix D, a nonzero fixed point exists if E satisfies both of the following inequalities:

$$E > E_{\text{lower}}(1+\eta) \tag{26}$$

and

$$E < \frac{K\cos\beta}{1+\cos\delta}, \tag{27}$$

where

$$\eta = \frac{K_c/K}{(2-K_c/K)(1+K\sin\beta)}. \tag{28}$$

We can find such E for $\beta \simeq 0$ and sufficiently large K when a value of δ is given. See Appendix D for details.

From Eq. (25) and (26), for $\Omega' > 0$, $\beta \simeq 0$, and sufficiently large K, it follows that the SN bifurcation should occur at $E \in [E_{\text{lower}}, E_{\text{lower}}(1+\eta)]$. As $\eta \to 0$ as $K \to \infty$, the bifurcation curve is well approximated by $E = E_{\text{lower}}$ for large K. In Fig. 2(c) we observe that E_{lower}, which is depicted as the approximate SN (aSN) curve, approximates the SN bifurcation curve well, although the sufficient condition given by Eqs. (26) and (27) cannot be satisfied in a range of δ.

Similarly to the SN bifurcation curve, the Hopf bifurcation curve is obtained by imposing $\mathrm{Tr}M = 0$ and $|M| > 0$. The former condition yields

$$E = \sqrt{\frac{\{Q_-^2 s^2 + [c+2\gamma(2R^{*2}+1)]^2 - 4\gamma^2 R^{*4}\}^2}{Q_+^2 Q_-^4 s^2} + \frac{16\gamma^2 R^{*4}}{Q_+^2 Q_-^2}}, \tag{29a}$$

$$\cos\delta = \frac{2[c+2\gamma(2R^{*2}+1)]}{EQ_+Q_-}, \tag{29b}$$

$$\sin\delta = -\frac{2s}{EQ_+} - \sqrt{1 - \frac{16\gamma^2 R^{*4}}{E^2 Q_+^2 Q_-^2}}, \tag{29c}$$

where

$$[c+2\gamma(2R^{*2}+1)]^2 - 4\gamma^2 R^{*4} + s^2 Q_-^2 \leqslant 0, \tag{30}$$

$$s = K(1+R^{*2})\sin\beta + 2, \tag{31}$$

$$c = K(-1+R^{*4})\cos\beta. \tag{32}$$

Inserting $0 < R^* < 1$ into Eqs. (29a), (29b), and (29c) and requiring $|M| > 0$ and Eq. (30) on the curve, we obtain the Hopf bifurcation curve. As shown in Appendix E, the Hopf bifurcation may also occur. However, as shown in Appendix F, we can exclude the possibility of this bifurcation for $\Omega' = 1 + K\sin\beta > 0$, as demonstrated in Fig. 2.

A codimension-two bifurcation occurs at which the curves PFs and PFu meet. A normal form of this bifurcation is known [37]. The weakly nonlinear analysis of our system performed in Appendix E implies that for $\Omega > 0$, a heteroclinic bifurcation curve extends from this point. The navy solid curve labeled by HC shows the heteroclinic bifurcation curve obtained using the software XPPAUT [38].

Figure 2 indicates that the heteroclinic bifurcation curve ends up at a point on the SN bifurcation curve, where another codimension-two bifurcation should occur. The observation of vector fields around this bifurcation point, shown in Fig. 3, reveals that the SN bifurcation curve is subdivided into two parts at this point, and the one labeled by SNIC in Fig. 2 corresponds to SN bifurcation on an invariant circle. A very similar codimension-two bifurcation is reported in [39], where SN, SNIC, and homoclinic bifurcation curves meet. We obtain a heteroclinic bifurcation curve rather than a homoclinic one because of the invariance of our system under $r \to -r$.

The three bifurcation curves HB, HC, and SNIC in Fig. 2 form the boundary of the stable synchronous state, provided that there is no other bifurcation involving periodic solutions, such as the SN bifurcation of limit cycles. Then the bistable region exists in the area surrounded by PFs, HC, and SN. Altogether, we obtain three qualitatively different phase diagrams depending on K values, as shown in Fig. 2. Our extensive numerical analysis performed in Sec. III C and Appendix G indicates that the phase diagrams given in Fig. 2 are comprehensive.

Other bifurcations may occur typically for $\Omega < 0$. As briefly mentioned in Appendix E, the codimension-two bifurcation at the intersection of Hopf, PFs, and PFu has a topologically different structure for $\Omega < 0$. The situation $\Omega < 0$ occurs for $-\frac{\pi}{2} < \beta < 0$ and sufficiently large K. In such a situation, in the absence of feedback, the mean field oscillates with a frequency opposite to the typical natural frequency of individual oscillators, i.e., $\omega_0 = 1$. This implies that synchronized individual oscillators also have frequencies opposite to their natural ones. However, such a phenomenon is not commonly observed in limit-cycle oscillators and should be regarded as an artifact owing to the use of phase approximation for a case of strong coupling. We therefore omit the case of $\Omega < 0$ in the present paper.

C. Numerical verification

To verify the analyses in Sec. III B, we simulated Eq. (6) for $N = 2000$. We set $\omega_i = \omega_0 + \gamma\tan[\frac{i\pi}{N} - \frac{(N+1)\pi}{2N}]$ with $\omega_0 = 1$, which converges to the Lorentzian distribution at $N \to \infty$ [40]. In Fig. 4(a) and its magnifications Figs. 4(b) and 4(c), we show the value of $\langle R\rangle$ for different feedback parameters, where the angle brackets denote the long-time

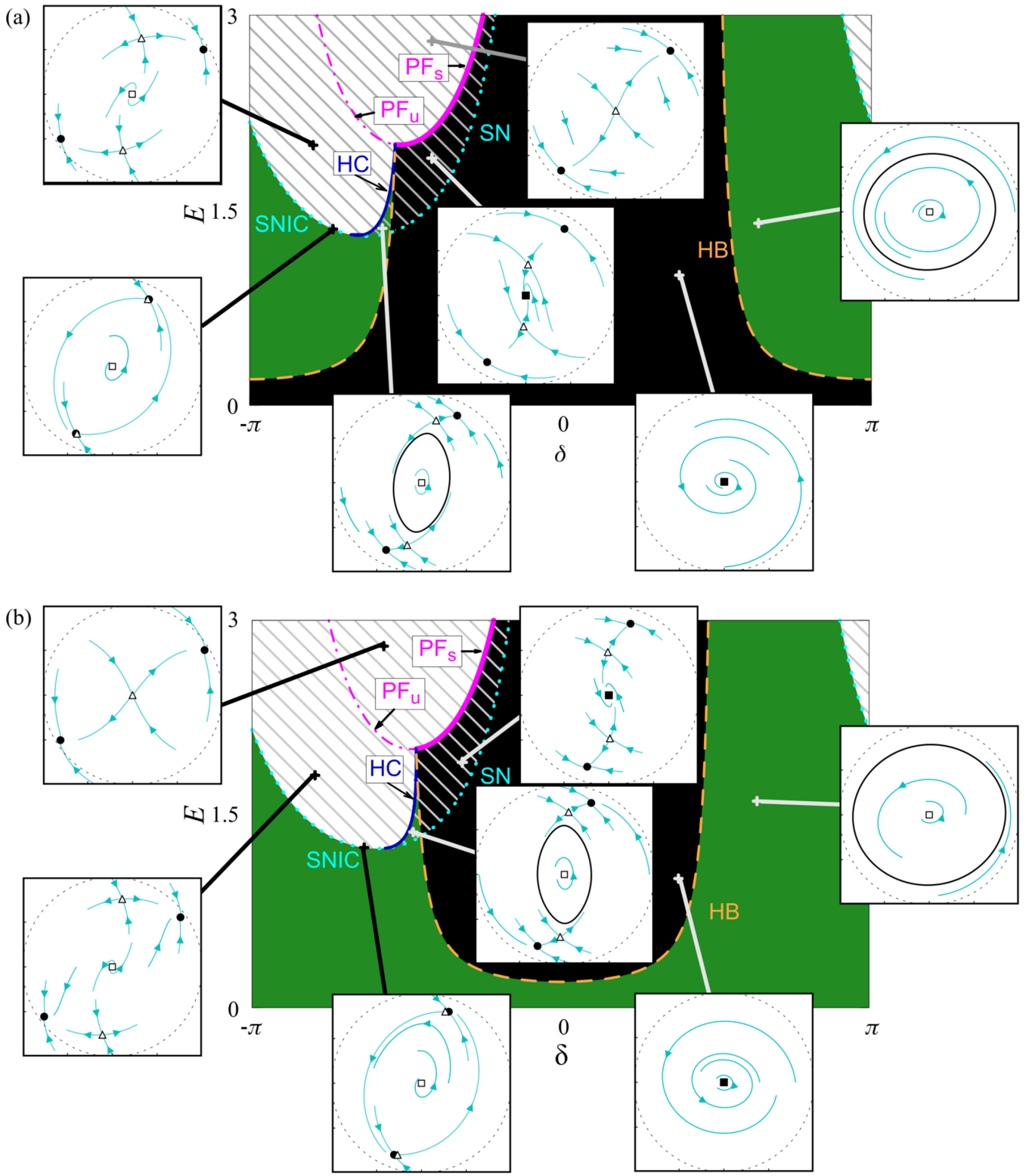

FIG. 3. Typical vector fields of Eq. (8) for different areas of the phase diagrams in Fig. 2. The vector fields on the complex planes are drawn with cyan arrows. Filled (resp. open) squares represent stable (resp. unstable) spirals, and filled (resp. open) circles represent stable (resp. unstable) nodes. The open triangles represent saddles. Stable limit cycles are illustrated using black solid curves. The circle drawn with the dashed line on each panel depicts the unit circle on the complex plane. The parameters for (a) and (b) are the same as those shown in Figs. 2(a) and 2(b), respectively.

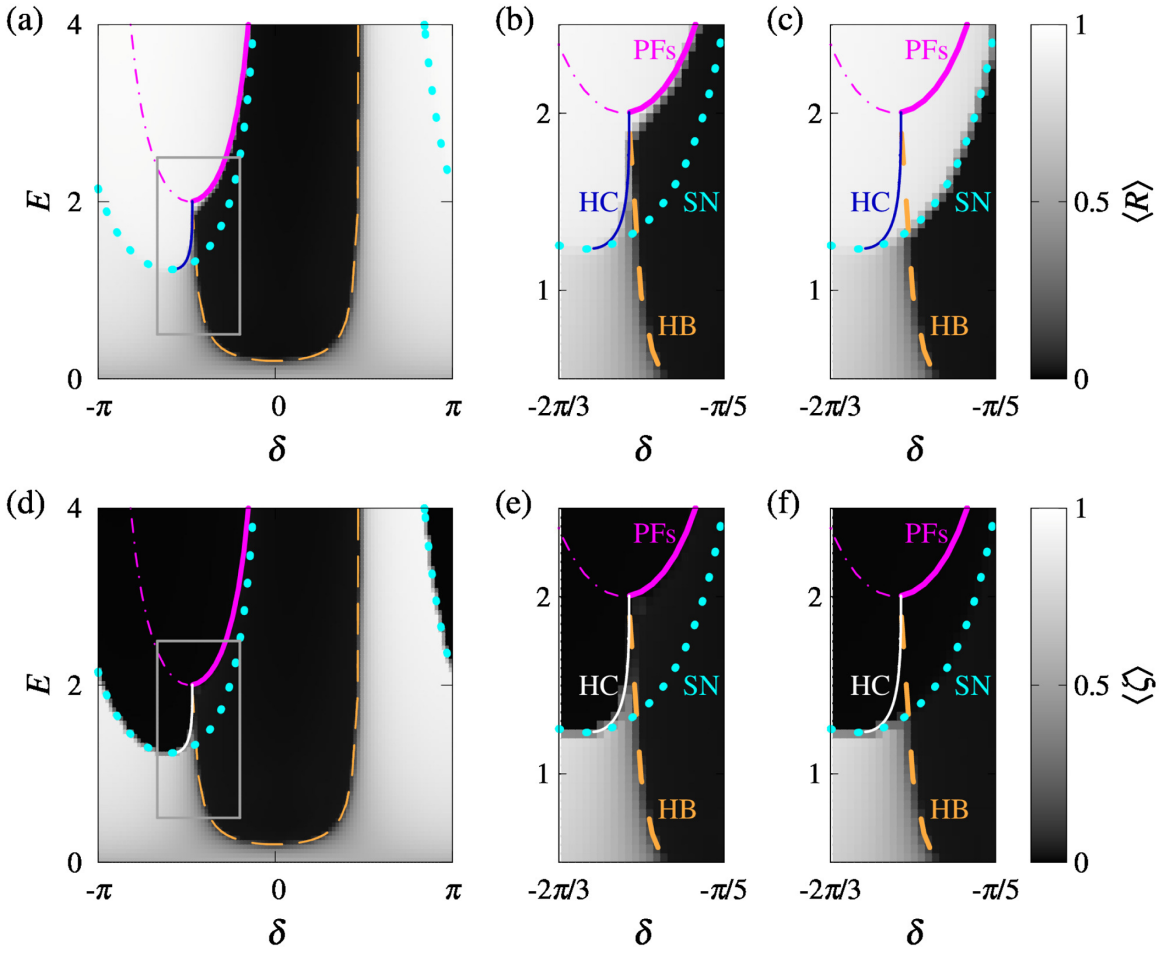

FIG. 4. Simulation results of Eq. (6). Long-time average of (a)–(c) R and (d)–(f) ζ. Parameters are the same as those in Fig. 2(b), and the same bifurcation curves are drawn here. The parameter range in (b), (c), (e), and (f) is the same as that in the boxed area in (a) and (d). The initial condition is the uniform phase distribution in (a), (b), (d), and (e) and the fully synchronized state in (c) and (f).

average. As the initial condition, we employ the uniform state, i.e., $\theta_i(0) = 2\pi(i-1)/N$ for $i = 1, \ldots, N$, in Figs. 4(a) and 4(b) and the fully synchronized state, i.e., $\theta_i(0) = 0$ for $i = 1, \ldots, N$, in Fig. 4(c). The parameters are the same as in Fig. 2(b), and we draw the same bifurcation curves in Figs. 4(a)–4(c) for comparison. Simulations with randomly drawn initial phases and natural frequencies are also carried out and indicate that such randomness does not qualitatively change the results. See Appendix H for details.

In the black regions in Fig. 4, $\langle R \rangle \simeq 0$ is obtained, which indicates that the system is in the asynchronous state. Because the initial condition employed in Figs. 4(a) and 4(b) is considered to be very close to the asynchronous state, the asynchronous state should be locally stable in the black region in Figs. 4(a) and 4(b), which is in excellent agreement with our prediction in Fig. 2(b).

Moreover, we can observe a discrepancy between Figs. 4(b) and 4(c) in the region surrounded by the curves SN, HB, and PFs, where the bistability between the asynchronous and oscillation-death states is predicted. To clarify which region of nonvanishing $\langle R \rangle$ in Fig. 2 corresponds to the synchronously oscillating or oscillation-death states, we further measure $\langle \zeta \rangle$, where $\zeta = |r - \langle r \rangle|$. From the definition of R and ζ, $\langle R \rangle > 0$ and $\langle \zeta \rangle = 0$ imply that the system is in the oscillation-death state, thus we confirm the predicted bistability as well as the existence of the stable oscillation-death state inside the SN and SNIC curves.

Owing to the symmetry of Eq. (8) under $r \to -r$, we obtain the pitchfork and heteroclinic bifurcation curves in Fig. 2. When this symmetry is weakly broken, similar bifurcations are expected to occur [37,41]. More specifically, SN and homoclinic bifurcation curves are expected to be obtained instead of the pitchfork and heteroclinic bifurcation curves, respectively. To numerically confirm that such asymmetry does not significantly alter the phase diagram, in Appendix I we investigate a variant of Eq. (8) in that a symmetry-breaking perturbation is introduced. The simulation results are similar to Fig. 4. See Appendix I for details.

IV. OPTIMAL FEEDBACK PARAMETERS

We consider $K > K_c$, or equivalently $\Lambda := -\gamma + \frac{K}{2}\cos\beta > 0$, for which the system falls into the synchronously oscillating state in the absence of the feedback, and determine the value of the phase offset δ that minimizes the required feedback strength E to suppress the synchronized oscillations. We can achieve this by leading the system to (1) the asynchronous state and (2) the oscillation-death

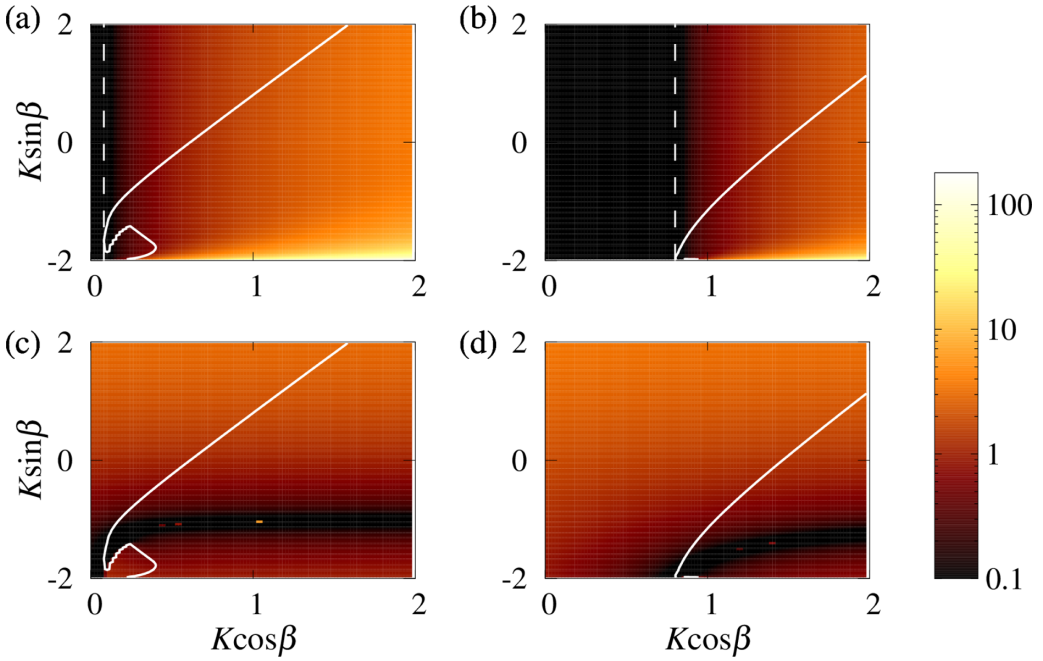

FIG. 5. Parameter dependency of (a), (b) $E_{\rm async}$ and (c), (d) $E_{\rm death}$. The solid lines represents the parameter values at which $E_{\rm death} = E_{\rm async}$ holds. (a), (c) $\gamma = 0.04$. (b), (d) $\gamma = 0.4$. On the left side of the dashed lines in (a) and (b), which depict $K\cos\beta = 2\gamma$, we have $E_{\rm async} = 0$ because the solution $r = 0$ is stable even without feedback.

state. Their optimal parameter sets (δ, E) are denoted by (1) $(\delta_{\rm async}, E_{\rm async})$ and (2) $(\delta_{\rm death}, E_{\rm death})$.

The point $(\delta_{\rm async}, E_{\rm async})$ can be determined analytically. Because the asynchronous state is stable for E above the HB curve and below the PFs curve, $(\delta_{\rm async}, E_{\rm async})$ is given by the minimum of the HB curve. Further, $\delta = 0$ provides the minimum when Eq. (15) holds for $\delta = 0$, resulting in

$$\delta_{\rm async} = 0, \tag{33a}$$

$$E_{\rm async} = 4\Lambda = -4\gamma + 2K\cos\beta. \tag{33b}$$

This is the case when $\Lambda \leqslant |\Omega| = |1 + \frac{K}{2}\sin\beta|$, which typically arises for small K or large $\tan\beta$. For $\Lambda > |\Omega|$, the smallest $|\delta|$ that satisfies Eq. (15) provides the minimum:

$$\delta_{\rm async} = \frac{\Omega}{|\Omega|}\arcsin\left(\frac{\Lambda^2 - \Omega^2}{\Lambda^2 + \Omega^2}\right), \tag{34a}$$

$$E_{\rm async} = \frac{2(\Lambda^2 + \Omega^2)}{|\Omega|}. \tag{34b}$$

Although $(\delta_{\rm death}, E_{\rm death})$ can only be numerically determined using Eqs. (22) and (29), an approximate expression can be obtained from (24):

$$\delta_{\rm death} \approx -\frac{\pi}{2}, \tag{35a}$$

$$E_{\rm death} \approx 1 + K\sin\beta. \tag{35b}$$

Figure 5 shows the parameter dependency of $E_{\rm async}$ given by Eqs. (33b) and (34b) and $E_{\rm death}$ obtained numerically using Eqs. (22) and (29). The general tendency is well captured by Eqs. (33b) and (35b). The solid lines represent the parameter set at which $E_{\rm async} = E_{\rm death}$. Based on Eqs. (33b) and (35b), we can roughly estimate that the asynchronous (oscillation-death) state can be achieved with a smaller feedback strength when $-4\gamma + 2K\cos\beta$ is small (large) compared to $1 + K\sin\beta$.

When we desire to suppress the collective oscillation without causing oscillation death, we need to consider the bistability between the asynchronous and oscillation-death states. For example, see Fig. 2(c), where $\delta_{\rm async} = 0$. Suppose that we increase E while fixing $\delta = 0$. Then, the oscillation-death state will be obtained before the asynchronous state. By further increasing E, we will eventually arrive at the HB curve, above which the asynchronous state is stable. However, because of the bistability, the oscillation-death state is expected to be sustained even in that region. Therefore, to realize the asynchronous state, we need to use a larger δ value at which we first arrive at the monostable region of the asynchronous state. Once the asynchronous state is realized, we can vary δ to $\delta = 0$ and decrease E to $E_{\rm async}$. To keep E as small as possible during the whole manipulation, we should employ a δ value close to that of the intersection of the HB and SN curves. Using the HB curve given by (14) and aSN curve given by Eq. (24), the approximate intersection can be found as

$$(\delta, E) \approx \left(\frac{\pi}{2} - 2\alpha, \frac{\Omega'^2 + 4\Lambda^2}{\Omega'^2}\right), \tag{36}$$

where

$$\alpha = \arcsin\left[\frac{\Omega'}{\sqrt{\Omega'^2 + 4\Lambda^2}}\right]. \tag{37}$$

Using this δ value, we can efficiently steer the system into the asynchronous state, as we demonstrate in Fig. 6.

Note that in contrast to the case of the stabilization of the asynchronous state, the feedback does not vanish when the oscillation-death state is achieved. Moreover, the minimum value of E does not necessarily imply that the intensity of the

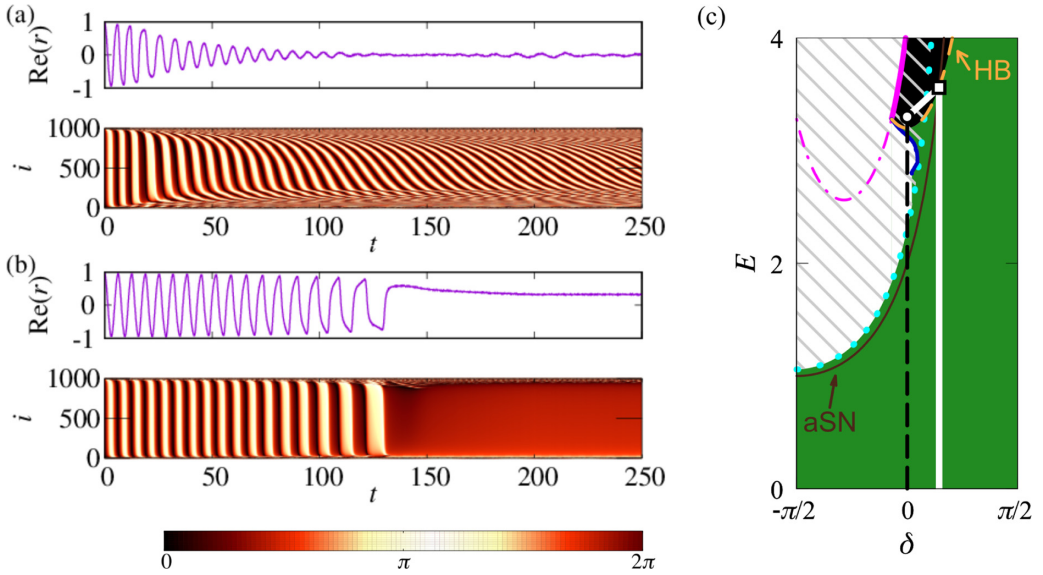

FIG. 6. Different macroscopic states are realized depending on how the feedback parameters δ and E are changed until they reach targeted values. In (a) and (b), the upper panel shows the time series of the real part of the complex order parameter, while the lower panel displays the phases of $N = 1000$ oscillators. Although the feedback parameters are set as $\delta = \delta_{\text{async}}$ and $E \simeq E_{\text{async}}$ at $t = 200$ in both (a) and (b), the path along which the feedback parameters are changed until $t = 200$ is different; in (a) the parameters are changed along the white solid line in (c), while in (b) the parameters are changed along the black dotted line in (c). This results in the different macroscopic states realized at $t = 250$. The asynchronous state is realized in (a), while the oscillation death state is realized in (b). The details of the path of the feedback parameters are as follows. In (a) the feedback parameters are set as $(\delta, E) = (\pi/2 - 2\alpha, 0)$ at $t = 0$, where α is given by Eq. (37). The feedback strength E is increased linearly with time until $t = 20$ to reach the E value at the intersection of HB curve and aSN curve, which is marked with open square in (c). Then δ and E are changed linearly so that δ becomes $0 = \delta_{\text{async}}$ and E becomes $3.3 \simeq E_{\text{async}}$ at $t = 200$. The point $(\delta, E) = (0, 3.3)$ is indicated by open circle in (c). In contrast, in (b) δ and E are set to δ_{async} and 0, respectively, at $t = 0$. Then E is increased linearly until it reaches $3.3 \simeq E_{\text{async}}$ at $t = 200$. For $t \geqslant 200$, the feedback parameters are kept constant in both (a) and (b). Other parameters are as follows: $\gamma = 0.1$, $\beta = 0$, and $K = 1.8 > K_c$. The natural frequencies and the initial conditions are set as $\omega_i = 1 + \gamma \tan[\frac{i\pi}{N} - \frac{(N+1)\pi}{2N}]$ and $\theta_i(0) = 0$, respectively, for $i = 1, 2, \ldots, N$.

feedback $|Ef(r)|$ is minimized as it also depends on r. Instead, this optimization does minimize the possible feedback intensity.

We perform numerical simulations of Eq. (6) to verify whether a near-optimal feedback properly works. Figure 7 shows the time series of the collective oscillation $\text{Re}(r(t))$ and the individual phases $\theta_i(t)$ before and after the onset of the feedback. In Fig. 7(a) the feedback with the parameters $E = 0.3 \approx E_{\text{async}}$ and $\delta = 0 = \delta_{\text{async}}$ is applied at $t = 5050$, as marked by the black arrow. Upon the onset of the feedback, the population begins to be desynchronized, and r decreases with time. In Fig. 7(b) the feedback parameters are chosen such that the oscillation-death state is induced with small feedback strength: $E = 1.10 \approx E_{\text{death}}$ and $\delta = -\pi/2 \approx \delta_{\text{death}}$. The figure indicates that the oscillations of the individual oscillators and the mean field terminate immediately because of the feedback.

V. INVESTIGATION ON THE ROBUSTNESS OF THE EFFECT OF FEEDBACK USING A DIFFERENT MODEL OF OSCILLATORS

Our analyses thus far are based on the model given by Eq. (6). As presented in Appendix A, this model is derived from a general class of coupled oscillator models. However, we assumed that coupling, inhomogeneity, and feedback are sufficiently weak to employ averaging approximations and that the functions contain only the first harmonics. Furthermore, we assumed the natural frequencies to obey Lorentzian distribution to obtain the reduced dynamical equation given in Eq. (8). Here, to exemplify the robustness of the results to the violation of these assumptions, we provide numerical results for a model with the form given by Eq. (A5). Specifically, we consider

$$\dot{\theta}_i = 1 + \mu_i \cos\theta_i + \frac{K}{N} Z_v(\theta_i) \sum_{j=1}^{N} V(\theta_j) + E Z_f(\theta_i) f(\boldsymbol{\theta}). \tag{38}$$

We adopt the pulse-like signal $V(\theta) = \nu_n (1 + \cos\theta)^n$ used in [42], where n is the parameter on the sharpness of V, and $\nu_n = 2^n (n!)^2/(2n)!$ normalizes $\int_0^{2\pi} V(\theta) d\theta$ to be 2π. We set $n = 10$. The phase sensitivity functions Z_v and Z_f are chosen to weakly include the second Fourier mode:

$$Z_v(\theta) = -\sin\theta + 0.2 \sin 2\theta, \tag{39}$$

$$Z_f(\theta) = \sin\theta + 0.2 \cos 2\theta. \tag{40}$$

Finally, μ_i is drawn from Gaussian distribution with mean 0 and standard deviation 0.1.

Numerical simulation of Eq. (38) for $N = 2000$ is conducted to calculate $\langle R \rangle$ and $\langle \zeta \rangle$, which are shown in

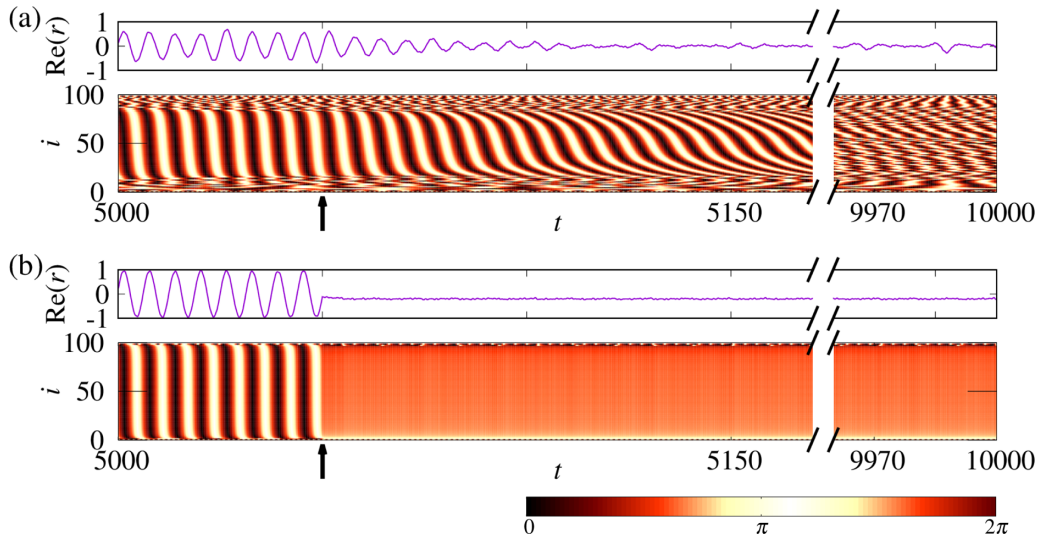

FIG. 7. Alteration of the dynamics of the $N = 100$ oscillators by the feedback. In each panel, the upper panel displays the time series of $\mathrm{Re}(r)$ while the lower panel shows the phases of the oscillators. (a) The feedback parameters are set as $E = 0.3 \approx E_{\mathrm{async}}$ and $\delta = 0 = \delta_{\mathrm{async}}$ to stabilize the asynchronous state with small E. The intrinsic parameters of the oscillators, K, β, and γ, are the same as those in Fig. 2(b). (b) The feedback parameters are set as $E = 1.1 \approx E_{\mathrm{death}}$ and $\delta = -\pi/2 \approx \delta_{\mathrm{death}}$ to induce the oscillation-death state with small E in the population that has the same parameters as Fig. 2(c).

Figs. 8(a) and 8(b), respectively. These figures qualitatively agree with Figs. 4(a) and 4(d), suggesting the robustness of the results.

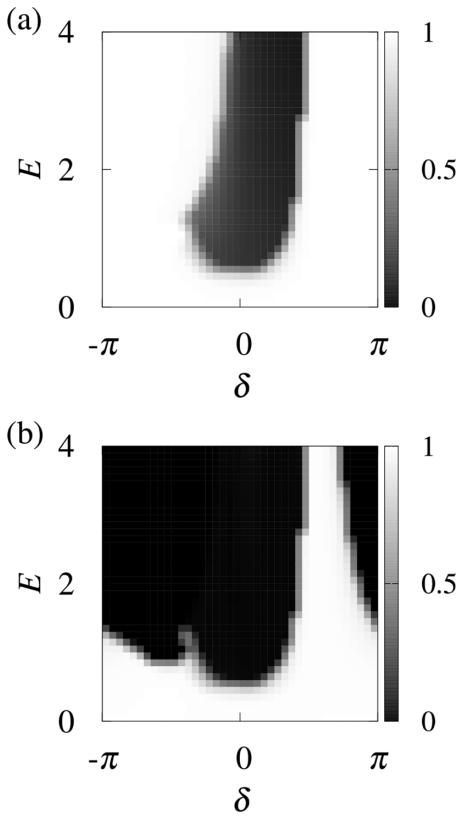

FIG. 8. Long-time average of (a) R and (b) ζ in the system of pulse-coupled oscillators under the feedback described by Eq. (38). Initial conditions are given by $\theta_i(0) = 2\pi(i-1)/N$. The coupling strength K is set to 0.3.

VI. CONCLUSION AND DISCUSSION

Motivated from the wide range of the applications of synchronization control, we analyzed an inhomogeneous population of phase oscillators exposed to global feedback. Detailed phase diagrams of the collective state are obtained based on the bifurcation analysis of the macroscopic equation derived using the Ott-Antonsen theory. The diagram displayed three types of macroscopic states: the synchronously oscillating state, the asynchronous state, and the oscillation-death state. Exact and approximate optimizations of the feedback parameters for steering a synchronously oscillating population into the asynchronous or the oscillation-death state with minimum feedback strength are also presented. Although we assumed several conditions such as the weakness of the coupling and the feedback in the derivation of the model equation, the numerical investigation in Sec. V demonstrates that our results do not change qualitatively even when some of the assumptions are violated to some extent.

Herein we focused on linear feedback F given by Eq. (2), and our extensive analysis revealed its utility for synchronization control. Linear feedback can be regarded as a basic methodology, and our study is expected to serve as a benchmark when more sophisticated feedback is to be designed. A natural extension is to make the feedback function F nonlinear in R. Although it will not change the linear stability of the asynchronous state, it may alter the stability and the existence of other states in addition to the amplitude of the collective oscillation [43]. A class of nonlinear feedback has been proposed in [23] for reducing the amplitude of the collective oscillation and further investigated in successive studies [43–47]. In [48,49], the authors showed that a class of delayed nonlinear feedback can stabilize complex dynamical states including a type of desynchronized state and demonstrated its ability to control electrochemical oscillators. Furthermore, regarding DBS, smooth feedback may not fulfill safety

requirements [50]. In [28], the authors compare two types of feedback: a smooth feedback and a series of pulses that are amplified according to the smooth feedback. They found that the pulses have a similar desynchronizing effect to the smooth feedback. The same approach might be applicable to the feedback studied in this article.

Our theoretical results can be demonstrated in some experimental systems. Recently, techniques for inferring phase dynamics and their interactions from observed oscillatory signals have been developed, and they have been utilized in experimental studies for predicting and controlling the dynamics of the oscillators [1,34,51–53]. These experiments have revealed various coupling and phase sensitivity functions; in some systems, the first Fourier component is dominant, while in other systems, some of the higher and the constant components are also prominent. In the former case, our analytical results may be verified quantitatively by estimating the values of ω_i, K, and β in Eq. (5) and implementing the global feedback loop. The feedback parameters δ and E can be tuned if R and Θ can be inferred online or two outputs from individual oscillators are available, as detailed in Appendix A.

As we noted in Sec. III C, our model has a particular symmetry; the dynamics of the complex order parameter, i.e., Eq. (8), is invariant under the change of $r \to -r$. This symmetry results from the invariance of the phase equation (5) under $\theta_i \to \theta_i + \pi$ for $i = 1, 2, \ldots, N$ because shifting the all the phases of oscillators by π results in changing r to $-r$. Hence, symmetry-breaking modifications to the phase equation can break the symmetry of the dynamics of r. There are several ways in which the symmetry of the phase equation is violated. The introduction of even-order harmonics in the phase sensitivity is one example. Modifications to the feedback function can also break the symmetry. For example, replacing $\cos(\theta_j - \delta)$ in the feedback function (2) with polynomials in $\cos(\theta_j - \delta)$ breaks the symmetry. Regarding the feedback function F that depends only on $r = Re^{i\Theta}$, the symmetry is kept if and only if $F(R, \Theta) = -F(R, \Theta + \pi)$ holds. As we shortly discussed in Sec. III C and detailed in Appendix I, the pitchfork and heteroclinic bifurcations may be replaced by other types of bifurcations in asymmetric systems. However, the simulation results in Appendix I indicate that the parameter region in that each macroscopic state is stable does not change significantly by weakly breaking the symmetry.

Finally, we remark on the limitation of the current study. It should be noted that our results are based on phase oscillator models. A qualitatively different phase diagram may be obtained for limit-cycle oscillators whose amplitudes considerably deviate from that of the unperturbed periodic orbit. Therefore, to understand the effect of a large amplitude deviation on synchronization control, it is important to investigate models of limit-cycle oscillators and compare them with our results.

ACKNOWLEDGMENTS

The authors thank Kei-Ichi Ueda for helpful discussions on numerical bifurcation analysis. H.K. acknowledges the financial support from JSPS KAKENHI Grant No. 18K11464.

H.K. conceived the study and supervised the project. A.O. performed the analytical and numerical investigations. A.O. wrote the manuscript with support from H.K.

APPENDIX A: DERIVATION OF OUR MODEL GIVEN IN EQ. (1)

We consider a general class of oscillator network given by

$$\dot{\boldsymbol{x}}_i = \boldsymbol{u}_i(\boldsymbol{x}_i; p_i, q_i), \tag{A1}$$

where $\boldsymbol{x}_i = (x_i, y_i, \ldots)$ and $\boldsymbol{u}_i$ $(i = 1, \ldots, N)$ are the state and the local vector field of the ith oscillator, respectively, and p_i and q_i are parameters. The interactions and external forcing are assumed to be given through variations in the parameters as $p_i = p_0 + \Delta p_i$ and $q_i = q_0 + \Delta q_i$, where p_0 and q_0 are the parameter values common for all the oscillators and Δp_i and Δq_i describe perturbations. When we consider global coupling and feedback, the perturbations may be given as

$$\Delta p_i = \frac{K'}{N} \sum_{j=1}^{N} v(\boldsymbol{x}_i, \boldsymbol{x}_j), \tag{A2}$$

$$\Delta q_i = \Delta q \equiv E' f(\boldsymbol{x}_1, \ldots, \boldsymbol{x}_N), \tag{A3}$$

where K' and E' are the strengths of coupling and feedback, respectively, and v and f are the functions describing coupling and feedback, respectively.

We follow the standard procedure of the phase reduction to obtain the corresponding phase description to Eq. (A1) [5,54]. Let us introduce $\Delta \boldsymbol{u}_i(\boldsymbol{x}_i; p_i, q_i) = \boldsymbol{u}_i(\boldsymbol{x}_i; p_i, q_i) - \boldsymbol{u}(\boldsymbol{x}_i; p_i, q_i)$ for $i = 1, \ldots, N$, which describes inhomogeneity in inherent oscillator properties. We assume that the unperturbed system,

$$\dot{\boldsymbol{x}} = \boldsymbol{u}(\boldsymbol{x}; p_0, q_0), \tag{A4}$$

has a stable limit cycle $\boldsymbol{x}^*(t)$. The phase of the unperturbed system is defined as a scalar field $\Phi(\boldsymbol{x})$ for the basin of attraction for the limit cycle such that the contour of $\Phi(\boldsymbol{x})$ describe the isochron of the unperturbed system [5,55]. Using this scalar field, the phase of the ith oscillator is defined as $\theta_i = \Phi(\boldsymbol{x}_i(t))$ $(i = 1, \ldots, N)$.

We assume that the orbital stability of the cycle $\boldsymbol{x}^*(t)$ in the unperturbed system given by Eq. (A4) is sufficiently higher than perturbation strength. Then, to the lowest order in perturbations strengths, each phase obeys

$$\dot{\theta}_i = \omega + \boldsymbol{Z}(\theta_i) \cdot \boldsymbol{U}_i(\theta_i) + \frac{K'}{N} \sum_{j=1}^{N} Z_v(\theta_i) V(\theta_i, \theta_j) + E' Z_f(\theta_i) F(\boldsymbol{\theta}), \tag{A5}$$

where ω is the natural frequency of the limit cycle $\boldsymbol{x}^*$; $\boldsymbol{U}_i$, V, F are the parametric representations of $\Delta \boldsymbol{u}_i$, v, f on the limit cycle $\boldsymbol{x}^*$ in terms of the phases, respectively; and $\boldsymbol{Z}, Z_v, Z_f$ are the phase sensitivity functions, which can be expressed in terms of the derivatives of $\boldsymbol{u}(\boldsymbol{x}; p, q)$ and $\Phi(\boldsymbol{x})$. All the functions are 2π-periodic in each argument.

When the magnitudes of the perturbation terms, i.e., the second to fourth terms of the right-hand side in Eq. (A5), are sufficiently small compared to ω, we may further simplify the equation using an averaging approximation. The resultant

equation is

$$\dot{\theta}_i = \omega + \Delta\omega_i + \frac{K'}{N}\sum_{j=1}^{N}\Gamma_v(\theta_i-\theta_j) + \frac{E'}{N}\sum_{j=1}^{N}\Gamma_f(\theta_i-\theta_j), \tag{A6}$$

where the constant $\Delta\omega_i$ and the functions Γ_v and Γ_f can be expressed in terms of the functions appearing in Eq. (A5). If the last term in Eq. (A5) is not very small compared to ω, we can still average the other terms to obtain

$$\dot{\theta}_i = \omega + \Delta\omega_i + \frac{K'}{N}\sum_{j=1}^{N}\Gamma_v(\theta_i-\theta_j) + E'Z_f(\theta_i)F(\boldsymbol{\theta}). \tag{A7}$$

In Eq. (A7), we may consider larger E' values than in Eq. (A6), which is the reason why we employ this type of model in this work.

Our model given in Eq. (1) is a version of Eq. (A7), where we assume that only the first harmonics are present in all the functions appearing in Eq. (A7), Γ_v, Z_f, and F. This assumption is valid when we consider limit-cycle oscillators close to a Hopf bifurcation point, in which the phase sensitivity and the wave forms are well approximated by the functions with only the first harmonics and with the constant and first harmonics terms, respectively. Let us further assume that from each oscillator we can observe two quantities, such as $x_j(t)$ and $y_j(t)$. If we denote the trajectory of the unperturbed limit cycle $\boldsymbol{x}^*(t)$ by $\boldsymbol{\chi}(\Phi)$, where $\boldsymbol{\chi}(\Phi(\boldsymbol{x}^*(t))) = \boldsymbol{x}^*(t)$, with its elements being $\boldsymbol{\chi} = (\chi_x, \chi_y, \ldots)$, the variation of $\chi_x(\theta)$ and $\chi_y(\theta)$ are almost sinusoidal near the Hopf bifurcation point. Therefore, the unperturbed waveforms can be denoted by $\chi_x(\theta) \simeq \bar{\chi}_x + A_x\cos(\theta-\delta_x)$ and $\chi_y(\theta) \simeq \bar{\chi}_y + A_y\cos(\theta-\delta_y)$, where $\bar{\chi}_x$ and $\bar{\chi}_y$ are the average of $\chi_x(\theta)$ and $\chi_y(\theta)$, respectively, A_x and A_y are the oscillation amplitudes, and δ_x and δ_y are the phase offsets in the waveforms. We then give the feedback function f as

$$f = \sum_{j=1}^{N}\left[a\frac{x_j-\bar{x}_j}{A_x} + b\frac{y_j-\bar{y}_j}{A_y}\right], \tag{A8}$$

where $\bar{x}_j$ and $\bar{y}_j$ denote the average values of x_j and y_j, respectively; and a and b are our control parameters. In the lowest order phase description, Eq. (A8) results in

$$F(\boldsymbol{\theta}) = \sum_{j=1}^{N}[a\cos(\theta_j-\delta_x) + b\cos(\theta_j-\delta_y)]. \tag{A9}$$

We can further transform (A9) to

$$F(\boldsymbol{\theta}) = \mathcal{E}\sum_{j=1}^{N}\cos(\theta_j-\delta), \tag{A10}$$

$$= \mathcal{E}R\cos(\Theta-\delta), \tag{A11}$$

where

$$\mathcal{E} = [(a\cos\delta_x + b\cos\delta_y)^2 + (a\sin\delta_x + b\sin\delta_y)^2]^{1/2}, \tag{A12}$$

$$\cos\delta = \frac{a\cos\delta_x + b\cos\delta_y}{\mathcal{E}}, \tag{A13}$$

$$\sin\delta = \frac{a\sin\delta_x + b\sin\delta_y}{\mathcal{E}}. \tag{A14}$$

We can give an arbitrary value of δ and an arbitrary non-negative value of $\mathcal{E}$ by appropriately choosing the values of a and b. This becomes clear when we describe $\mathcal{E}$ and $\tan\delta$ in terms of a/b:

$$\mathcal{E} = |b|\left[\left(\frac{a}{b}\cos\delta_x + \cos\delta_y\right)^2 + \left(\frac{a}{b}\sin\delta_x + \sin\delta_y\right)^2\right]^{1/2}, \tag{A15}$$

$$\tan\delta = \frac{(a/b)\sin\delta_x + \sin\delta_y}{(a/b)\cos\delta_x + \cos\delta_y}. \tag{A16}$$

Equation (A16) implies that $\tan\delta$ can be tuned to any values by varying a/b because it is a hyperbola as a function of a/b, whereas Eq. (A15) implies that $\mathcal{E}$ can be tuned to any non-negative value by keeping a/b constant and varying b. Furthermore, from Eqs. (A13) and (A14), it follows that δ is shifted by π when the signs of a and b are reversed. Therefore, $\mathcal{E}$ takes arbitrary non-negative values and δ takes arbitrary values. Because $\tilde{E}$ in Eq. (1) is given by $\tilde{E} = E'\mathcal{E}$, $\tilde{E} \geqslant 0$ can also be set arbitrarily.

APPENDIX B: CLASSIFICATION OF THE ZERO-EIGENVALUE BIFURCATION AT THE ORIGIN

The codimension-one bifurcation involving a zero eigenvalue at the origin is limited to the pitchfork bifurcation. One possible approach for this is to consider the facts that the SN bifurcation may not occur because the constant solution $r = 0$ may not vanish in Eq. (8) and the pitchfork bifurcation rather than the transcritical bifurcation occurs because the symmetry of Eq. (8) implies that the emergence of a constant solution $r = r^* \neq 0$ must be accompanied with the emergence of $r = -r^*$ as well.

An alternative way is to perform the center manifold reduction [37], which will clarify that the bifurcation is actually the pitchfork one and whether the bifurcation is super- or subcritical. Let the bifurcation parameter be $\mu = E - E_{\rm pf}$, where $E_{\rm pf}$ is given by Eq. (16). Inserting $r = u + iv$ and $E = E_{\rm pf} + \mu$ into Eq. (8), we obtain

$$\begin{pmatrix}\dot{u}\\ \dot{v}\end{pmatrix} = \begin{pmatrix}\Lambda - \frac{E_{\rm pf}\cos\delta}{2} & -\Omega - \frac{E_{\rm pf}\sin\delta}{2}\\ \Omega & \Lambda\end{pmatrix}\begin{pmatrix}u\\ v\end{pmatrix} + \begin{pmatrix}p(u,v)\\ q(u,v)\end{pmatrix}, \tag{B1}$$

where

$$\begin{aligned} p(u,v) = &-\frac{\mu}{2}(u\cos\delta + v\sin\delta)\\ &+\frac{E_{\rm pf}+\mu}{2}(u^2-v^2)(u\cos\delta + v\sin\delta)\\ &-\frac{K}{2}(u^2+v^2)(u\cos\beta + v\sin\beta), \end{aligned} \tag{B2}$$

$$\begin{aligned} q(u,v) = &\, u^2v[(E_{\rm pf}+\mu)\cos\delta - \gamma - \Lambda]\\ &+uv^2[(E_{\rm pf}+\mu)\sin\delta + \Omega - 1]\\ &+u^3(\Omega-1) + v^3(-\gamma-\Lambda). \end{aligned} \tag{B3}$$

To reduce the system, let us transform the variables as follows:

$$\begin{pmatrix}u\\ v\end{pmatrix} = \begin{pmatrix}-\frac{\Lambda}{\Omega} & \frac{\Lambda\sin\delta+\Omega\cos\delta}{\Omega\sin\delta-\Lambda\cos\delta}\\ 1 & 1\end{pmatrix}\begin{pmatrix}\hat{u}\\ \hat{v}\end{pmatrix}, \tag{B4}$$

which yields

$$\begin{pmatrix}\dot{\hat{u}}\\ \dot{\hat{v}}\end{pmatrix}=\begin{pmatrix}0 & 0\\ 0 & \hat{\lambda}\end{pmatrix}\begin{pmatrix}\hat{u}\\ \hat{v}\end{pmatrix}+\begin{pmatrix}a_1\mu\hat{u}+a_2\mu\hat{v}+a_3\hat{u}^3+O(v^3,uv^2,u^2v)\\ b\mu\hat{u}+O(\mu\hat{v},\hat{v}^3,\hat{u}\hat{v}^2,\hat{u}^2\hat{v},\hat{u}^3)\end{pmatrix}, \tag{B5}$$

where

$$\hat{\lambda}=\frac{\cos\delta(\Lambda^2-\Omega^2)-2\Lambda\Omega\sin\delta}{\Lambda\cos\delta-\Omega\sin\delta}, \tag{B6}$$

$$a_1=\frac{(\Omega\sin\delta-\Lambda\cos\delta)^2}{2[(\Omega^2-\Lambda^2)\cos\delta+2\Lambda\Omega\sin\delta]}, \tag{B7}$$

$$a_2=\frac{\Omega^2}{2[(\Omega^2-\Lambda^2)\cos\delta+2\Lambda\Omega\sin\delta]}, \tag{B8}$$

$$a_3=\frac{(\Lambda^2+\Omega^2)\{(-2\gamma\Lambda\Omega+\Lambda^2-\Omega^2)\sin\delta+[\gamma(\Lambda^2-\Omega^2)+2\Lambda\Omega]\cos\delta\}}{\Omega^2[(\Omega^2-\Lambda^2)\cos\delta+2\Lambda\Omega\sin\delta]}, \tag{B9}$$

$$b_1=\frac{(\Lambda\cos\delta-\Omega\sin\delta)^2}{2(\Lambda^2-\Omega^2)\cos\delta-4\Lambda\Omega\sin(\delta)}. \tag{B10}$$

Equation (B5) implies that $\hat{\lambda}<0$ is required for the origin to lose its stability through the codimension-one bifurcation at $\mu=0$. The center manifold $\hat{v}=c(\hat{u},\mu)$ up to the second order is given by

$$c(\hat{u},\mu)=-\frac{b}{\hat{\lambda}}\mu\hat{u}+O(\hat{u}\mu^2,\hat{u}^3). \tag{B11}$$

On this center manifold, the dynamics is reduced to

$$\dot{\hat{u}}=a_1\mu\left(1-\frac{a_2b}{\hat{\lambda}a_1}\mu\right)\hat{u}+a_3\hat{u}^3+O(\mu\hat{u}^3,\mu^3\hat{u}). \tag{B12}$$

Equation (B12) implies that the pitchfork bifurcation occurs at $\mu=0$. It is supercritical for $a_3<0$ and subcritical for $a_3>0$.

Below, we show that the bifurcation is subcritical when $\hat{\lambda}<0$, $\Omega>0$, and $E_{\rm pf}$ is sufficiently small compared to Ω/γ. Because $E\geqslant 0$, and the numerator of $E_{\rm pf}$ is positive, the denominator of $E_{\rm pf}$ is also positive:

$$\Lambda\cos\delta-\Omega\sin\delta>0, \tag{B13}$$

which implies that the denominator of $\hat{\lambda}$ is positive. Thus, if $\hat{\lambda}<0$, the numerator of $\hat{\lambda}$ is negative:

$$(\Lambda^2-\Omega^2)\cos\delta-2\Lambda\Omega\sin\delta<0. \tag{B14}$$

Under this condition, a_3 is positive if

$$[\gamma(\Lambda^2-\Omega^2)+2\Lambda\Omega]\cos\delta>(2\gamma\Lambda\Omega-\Lambda^2+\Omega^2)\sin\delta, \tag{B15}$$

$$\Longleftrightarrow\ \Omega(\Lambda\cos\delta-\Omega\sin\delta)>-\Lambda(\Lambda\sin\delta+\Omega\cos\delta)+\gamma[2\Lambda\Omega\sin\delta-(\Lambda^2-\Omega^2)\cos\delta]. \tag{B16}$$

We first consider the case of $\Lambda\geqslant 0$. Then, the first term of the right-hand side of Eq. (B16) is negative because Eqs. (B13) and (B14) yield

$$0\leqslant\Lambda(\Lambda\cos\delta-\Omega\sin\delta)<\Omega(\Lambda\sin\delta+\Omega\cos\delta). \tag{B17}$$

As for the second term, noting that $|\cos\delta|,\ |\sin\delta|\leqslant 1$, we obtain

$$2\Lambda\Omega\sin\delta-(\Lambda^2-\Omega^2)\cos\delta\leqslant 2\Lambda\Omega+\Lambda^2+\Omega^2\leqslant 2(\Lambda^2+\Omega^2). \tag{B18}$$

Equations (B16), (B17), and (B18) yield the following sufficient condition for a_3 to be positive:

$$\Omega(\Lambda\cos\delta-\Omega\sin\delta)>2\gamma(\Lambda^2+\Omega^2), \tag{B19}$$

which is equivalent to

$$E_{\rm pf}=\frac{2(\Lambda^2+\Omega^2)}{\Lambda\cos\delta-\Omega\sin\delta}<\frac{\Omega}{\gamma}. \tag{B20}$$

Therefore, for $\Lambda\geqslant 0$, the bifurcation is subcritical when $E_{\rm pf}$ is sufficiently small compared to Ω/γ.

We next consider the case of $\Lambda<0$. If $\Lambda\sin\delta+\Omega\cos\delta<0$ holds, we can derive Eq. (B20) in the same manner as the case of $\Lambda\geqslant 0$. When $\Lambda\sin\delta+\Omega\cos\delta\geqslant 0$, we evaluate the right-hand side of Eq. (B16) as follows. As $|\Lambda|<\gamma$ holds for $\Lambda<0$,

$$-\Lambda(\Lambda\sin\delta+\Omega\cos\delta)<\gamma(|\Lambda|+\Omega). \tag{B21}$$

This equation and Eqs. (B16) and (B18) yield the sufficient condition for the subcritical bifurcation

$$\Omega(\Lambda\cos\delta-\Omega\sin\delta)>2\gamma(\Lambda^2+\Omega^2)\left[1+\frac{|\Lambda|+\Omega}{2(\Lambda^2+\Omega^2)}\right], \tag{B22}$$

which is equivalent to

$$E_{\rm pf}<\frac{\Omega}{\gamma\left[1+\frac{|\Lambda|+\Omega}{2(\Lambda^2+\Omega^2)}\right]}. \tag{B23}$$

From Eq. (B20) and Eq. (B23), it is shown that the pitchfork bifurcation is subcritical if $E_{\rm pf}$ is sufficiently small compared to Ω/γ.

Near the parameter regions considered in Fig. 2, $E_{\rm pf}$ is small enough, and hence the pitchfork bifurcation involving a stable fixed point is subcritical.

APPENDIX C: WEAKLY NONLINEAR ANALYSIS OF THE HOPF BIFURCATION

We show below that the Hopf bifurcation at the origin is always supercritical. Substituting $r=u+iv$ and the value

of the feedback strength at the bifurcation point, given by Eq. (14), into Eq. (8), we have

$$\begin{pmatrix}\dot{u}\\ \dot{v}\end{pmatrix}=\begin{pmatrix}-\Lambda & -2\Lambda\tan\delta-\Omega\\ \Omega & \Lambda\end{pmatrix}\begin{pmatrix}u\\ v\end{pmatrix}+\begin{pmatrix}g(u,v)\\ h(u,v)\end{pmatrix}, \quad \text{(C1)}$$

where

$$g(x,y)=2\Lambda(x^2-y^2)(x+y\tan\delta) - \frac{K}{2}(x^2+y^2)(x\cos\beta+y\sin\beta), \quad \text{(C2)}$$

$$h(x,y)=\tfrac{K}{2}(x^2+y^2)(x\sin\beta-y\cos\beta)+4\Lambda xy(x+y\tan\delta). \quad \text{(C3)}$$

To simplify the calculation, we change the coordinates to

$$\begin{pmatrix}\tilde{u}\\ \tilde{v}\end{pmatrix}=\begin{pmatrix}\Omega/\tilde{\omega} & \Lambda/\tilde{\omega}\\ 0 & 1\end{pmatrix}\begin{pmatrix}u\\ v\end{pmatrix}, \quad \text{(C4)}$$

where $\tilde{\omega}=\sqrt{-\Lambda^2+\Omega^2+2\Lambda\Omega\tan\delta}$. Then $\tilde{u}$ and $\tilde{v}$ obey

$$\begin{pmatrix}\dot{\tilde{u}}\\ \dot{\tilde{v}}\end{pmatrix}=\begin{pmatrix}0 & -\tilde{\omega}\\ \tilde{\omega} & 0\end{pmatrix}\begin{pmatrix}\tilde{u}\\ \tilde{v}\end{pmatrix}+\begin{pmatrix}\tilde{g}(\tilde{u},\tilde{v})\\ \tilde{h}(\tilde{u},\tilde{v})\end{pmatrix}, \quad \text{(C5)}$$

where

$$\begin{pmatrix}\tilde{g}(\tilde{u},\tilde{v})\\ \tilde{h}(\tilde{u},\tilde{v})\end{pmatrix}=\begin{pmatrix}\Omega/\tilde{\omega} & \Lambda/\tilde{\omega}\\ 0 & 1\end{pmatrix}\begin{pmatrix}g(u(\tilde{u},\tilde{v}),v(\tilde{u},\tilde{v}))\\ h(u(\tilde{u},\tilde{v}),v(\tilde{u},\tilde{v}))\end{pmatrix}. \quad \text{(C6)}$$

Then $z=\tilde{u}+i\tilde{v}$ obeys

$$\dot{z}=i\tilde{\omega}z+\tilde{g}+i\tilde{h}. \quad \text{(C7)}$$

Using a near-identity transformation, Eq. (C7) is further reduced to the following normal form of the Hopf bifurcation [37]:

$$\dot{w}=i\tilde{\omega}w+d|w|^2w+O(|w|^5), \quad \text{(C8)}$$

where $w, d\in\mathbb{C}$, and

$$\mathrm{Re}(d)=-\gamma\left(1+\frac{\Lambda}{\Omega}\tan\delta\right). \quad \text{(C9)}$$

The bifurcation is supercritical when $\mathrm{Re}(d)<0$. Noting that $\gamma>0$, we may further show $\mathrm{Re}(d)<0$ as follows. When $\frac{\Lambda}{\Omega}\tan\delta\geqslant 0$, it is obvious that $\mathrm{Re}(d)<0$ from Eq. (C9). When $\frac{\Lambda}{\Omega}\tan\delta<0$, the following inequality holds:

$$1+\frac{\Lambda}{\Omega}\tan\delta>1+2\frac{\Lambda}{\Omega}\tan\delta. \quad \text{(C10)}$$

Moreover, Eq. (15) implies that the Hopf bifurcation at the origin occurs only when

$$-\Lambda^2+\Omega^2+2\Lambda\Omega\tan\delta>0. \quad \text{(C11)}$$

From Eqs. (C10) and (C11), we have

$$1+\frac{\Lambda}{\Omega}\tan\delta>\left(\frac{\Lambda}{\Omega}\right)^2>0, \quad \text{(C12)}$$

and hence $\mathrm{Re}(d)<0$. Therefore, the Hopf bifurcation at the origin is supercritical for any parameter values.

APPENDIX D: DERIVATION OF THE SUFFICIENT CONDITION FOR A NONZERO FIXED POINT

Here, under the conditions $K>2K_c$ and $\Omega'=1+K\sin\beta>0$, we derive Eqs. (26) and (27), i.e., a sufficient condition for Eq. (18) to have a nonzero fixed point. Note that an intersection of the two nullclines

$$-\gamma+(1-R^2)\left\{\frac{K}{2}\cos\beta-\frac{E}{4}[\cos(\delta-2\Theta)+\cos\delta]\right\}=0 \quad \text{(D1)}$$

and

$$1+(1+R^2)\left\{\frac{K}{2}\sin\beta+\frac{E}{4}[\sin\delta-\sin(\delta-2\Theta)]\right\}=0 \quad \text{(D2)}$$

gives a nonzero fixed point. Thus there exists a fixed point (R^*,Θ^*) such that $R_{\mathrm{lower}}<R^*<1$ if both of the following conditions are satisfied: (1) the nullcline given by Eq. (D1) is defined for any Θ, and the value of R on the nullcline always satisfies $R_{\mathrm{lower}}<R^*<1$, and (2) the nullcline given by Eq. (D2) passes through the region $R_{\mathrm{lower}}<R^*<1$ on the R-Θ plane.

The first condition is equivalent to that the following inequality holds for any Θ:

$${R_{\mathrm{lower}}}^2<1-\frac{4\gamma}{2K\cos\beta-E[\cos(\delta-2\Theta)+\cos\delta]}<1, \quad \text{(D3)}$$

which is satisfied when

$$E<\frac{2K\cos\beta-4\gamma(1-{R_{\mathrm{lower}}}^2)^{-1}}{1+\cos\delta}. \quad \text{(D4)}$$

Next we discuss the second condition. Equation (D2) yields $R^2=-1+S(\sin(\delta-2\Theta))^{-1}$, where

$$S(x)=-\frac{K}{2}\sin\beta+\frac{E}{4}(x-\sin\delta) \quad \text{(D5)}$$

is a monotonically increasing function of x. Because $\sin(\delta-2\Theta)$ is in the range of $[-1,1]$, the nullcline given by Eq. (D2) crosses over the region $R_{\mathrm{lower}}<R^*<1$ if

$$S(-1)<\tfrac{1}{2} \quad \text{(D6)}$$

and

$$S(1)>\left(1+R_{\mathrm{lower}}^2\right)^{-1}. \quad \text{(D7)}$$

When $\Omega'>0$, the inequality given by (D6) holds for any $E\geqslant 0$. In contrast, inequality (D7) holds when

$$E>E_{\mathrm{lower}}\left[1+\frac{1-{R_{\mathrm{lower}}}^2}{(1+{R_{\mathrm{lower}}}^2)(1+K\sin\beta)}\right], \quad \text{(D8)}$$

where E_{lower} is given by Eq. (24).

Therefore, if Eqs. (D4) and (D8) are satisfied, a nonzero fixed point (R^*,Θ^*) that satisfies $R_{\mathrm{lower}}<R^*<1$ exists. As a special case, we obtain Eqs. (26) and (27), respectively, by setting $R_{\mathrm{lower}}=\sqrt{1-\frac{2K_c}{K}}$ in Eqs. (D8) and (D4).

We can find a value of E that satisfies both of Eqs. (26) and (27) when

$$E_{\text{lower}}(1+\eta) < \frac{K\cos\beta}{1+\cos\delta}, \tag{D9}$$

which is equivalent to

$$\frac{2}{1-\sin\delta}\left(\frac{1}{K-K_c}+\sin\beta\right)-\frac{\cos\beta}{1+\cos\delta}<0. \tag{D10}$$

Equation (D10) holds when $\beta \simeq 0$ and K is sufficiently large for a given value of δ.

APPENDIX E: ANALYSIS ON THE CODIMENSION-TWO BIFURCATION POINT

By imposing $\mathrm{Tr}L = |L| = 0$, we obtain the values of the feedback parameters at which the Hopf bifurcation curve (14) and the pitchfork bifurcation curve (16) meet as

$$\sin\delta = \frac{\Omega}{|\Omega|}\frac{\Lambda^2-\Omega^2}{\Lambda^2+\Omega^2}, \tag{E1}$$

$$\cos\delta = \frac{2\Lambda|\Omega|}{\Lambda^2+\Omega^2}, \tag{E2}$$

$$E = \frac{2(\Lambda^2+\Omega^2)}{|\Omega|}. \tag{E3}$$

Substituting $r = u + iv$ together with Eq. (E1)–(E3) into Eq. (8), we have

$$\begin{pmatrix}\dot u\\ \dot v\end{pmatrix} = \begin{pmatrix}-\Lambda & -\frac{\Lambda^2}{\Omega}\\ \Omega & \Lambda\end{pmatrix}\begin{pmatrix}u\\ v\end{pmatrix} + \begin{pmatrix}g_2(u,v)\\ h_2(u,v)\end{pmatrix}, \tag{E4}$$

where

$$g_2(u,v) = (\Lambda-\gamma)u^3 + \left(1-2\Omega+\frac{\Lambda^2}{\Omega}\right)u^2v - (\gamma+3\Lambda)uv^2 + \left(1-\frac{\Lambda^2}{\Omega}\right)v^3, \tag{E5}$$

$$h_2(u,v) = (\Omega-1)u^3 - (\gamma-3\Lambda)u^2v + \left(-1-\Omega+\frac{2\Lambda^2}{\Omega}\right)uv^2 - (\gamma+\Lambda)v^3. \tag{E6}$$

Next, we transform the linear part into the Jordan normal form by the following change of variables:

$$\begin{pmatrix}\check u\\ \check v\end{pmatrix} = \begin{pmatrix}0 & 1\\ \Omega & \Lambda\end{pmatrix}\begin{pmatrix}u\\ v\end{pmatrix}, \tag{E7}$$

which yields

$$\begin{pmatrix}\dot{\check u}\\ \dot{\check v}\end{pmatrix} = \begin{pmatrix}\check v\\ 0\end{pmatrix} + \begin{pmatrix}c_1\check u^3 + c_2\check u^2\check v + c_3\check u\check v^2 + c_4\check v^3,\\ d_1\check u^3 + d_2\check u^2\check v + d_3\check u\check v^2 + d_4\check v^3\end{pmatrix}, \tag{E8}$$

where

$$c_1 = (\Lambda^2+\Omega^2)(\Lambda-\gamma\Omega)/\Omega^3, \tag{E9}$$

$$c_2 = (2\gamma\Lambda\Omega - \Lambda^2\Omega - 3\Lambda^2 - \Omega^2 - \Omega^3)/\Omega^3, \tag{E10}$$

$$c_3 = (3\Lambda-\gamma\Omega)/\Omega^3, \tag{E11}$$

$$c_4 = (-1+\Omega)/\Omega^3, \tag{E12}$$

$$d_1 = (\Lambda^2+\Omega^2)^2/\Omega^3, \tag{E13}$$

$$d_2 = (\Lambda^2+\Omega^2)(-\gamma\Omega-3\Lambda)/\Omega^3, \tag{E14}$$

$$d_3 = [(3\Lambda^2+\Omega^2) - 2\Omega(-\gamma\Lambda+\Lambda^2+\Omega^2)]/\Omega^3, \tag{E15}$$

$$d_4 = [-\Lambda-\Omega(\gamma-2\Lambda)]/\Omega^3. \tag{E16}$$

Equation (E8) is then reduced to

$$\begin{pmatrix}\dot U\\ \dot V\end{pmatrix} = \begin{pmatrix}V\\ 0\end{pmatrix} + \begin{pmatrix}0\\ d_1U^3 + (3c_1+d_2)U^2V\end{pmatrix} + O(U^5, U^4V, U^3V^2, U^2V^3, UV^4, V^5) \tag{E17}$$

by the following near-identity transformation:

$$\begin{pmatrix}\check u\\ \check v\end{pmatrix} = \begin{pmatrix}U\\ V\end{pmatrix} + \begin{pmatrix}\frac{1}{6}(2c_2+d_3)U^3 + \frac{1}{2}(c_3+d_4)U^2V + c_4UV^2\\ -c_1U^3 + \frac{1}{2}d_3U^2V + d_4UV^2\end{pmatrix}. \tag{E18}$$

The signs of d_1 and $d_2' := 3c_1 + d_2 = -4\gamma(\Lambda^2+\Omega^2)/\Omega^2$ determine the types of the codimension-one bifurcation that occurs near the codimension-two bifurcation point [37]. The heteroclinic bifurcation as well as the Hopf and the pitchfork bifurcations occurs for $d_1d_2' < 0$, while the bifurcation involving a pair of homoclinic orbit occurs for $d_1d_2' > 0$ [37]. The former is the case for $\Omega > 0$, and the latter is the case for $\Omega < 0$.

Note that the analysis above only gives the information around a specific codimension-two bifurcation point and does not necessarily imply that the Hopf bifurcation involving nonzero fixed point may not occur for $\Omega > 0$. In practice, we numerically observed it for some parameter sets even when $\Omega > 0$. However, as detailed in Appendix F,

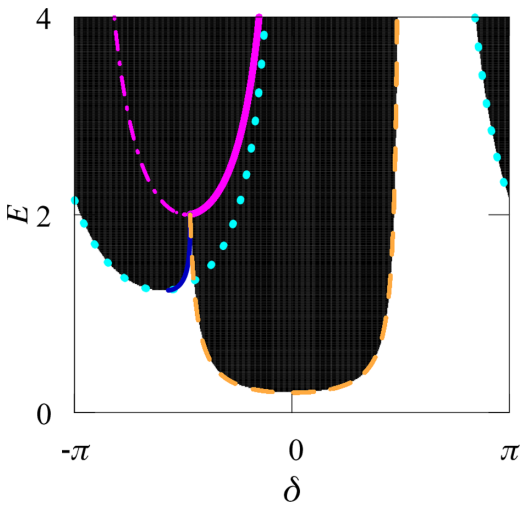

FIG. 9. The stable region of the limit-cycle solution. The region where at least one stable limit cycle exists is filled with black. The bifurcation curves obtained in Sec. III are also plotted. The Hopf, SNIC, and heteroclinic bifurcation curves agree with the boundary of the black region. The parameters are the same as those in Fig. 2(b).

we can show that this bifurcation does not occur for $\Omega' = 1 + K\sin\beta > 0$.

APPENDIX F: ABSENCE OF HOPF BIFURCATION INVOLVING A NONZERO FIXED POINT FOR $\Omega' > 0$

In this Appendix, we show that Hopf bifurcation involving a nonzero fixed point does not occur for $\Omega' > 0$. A necessary condition for this bifurcation to occur is that the stability matrix M given by Eq. (19) satisfies $|M| > 0$ and $\mathrm{Tr}M = 0$. Therefore, it is sufficient to show that $|M| \leqslant 0$ holds when $\mathrm{Tr}M = 0$.

The condition $\mathrm{Tr}M = 0$ yields

$$\frac{E}{2}(R^{*2}+1)\cos(\delta - 2\Theta^*) = \frac{2R^{*2}\gamma}{1-R^{*2}}. \tag{F1}$$

Substituting Eq. (F1) into Eq. (19), we obtain

$$|M| = -\left[\frac{E}{2}(R^{*2}+1)\cos(\delta-2\Theta^*)\right]^2 - \frac{E(1-R^{*2})R^{*2}\sin(\delta-2\Theta^*)}{1+R^{*2}} \tag{F2}$$

$$= m_2(R^*)\sin^2(\delta-2\Theta^*) + m_1(R^*)\sin(\delta-2\Theta^*) + m_0(R^*) \tag{F3}$$

$$\equiv D(\sin(\delta-2\Theta^*);R^*), \tag{F4}$$

where

$$m_2(R^*) = -m_0(R^*) = \frac{E^2(1+R^{*2})^2}{4}, \tag{F5}$$

$$m_1(R^*) = -\frac{E(1-R^{*2})R^{*2}}{1+R^{*2}}. \tag{F6}$$

Because $D(s;R^*)$ is a quadratic function of s, we can solve $D(s;R^*) = 0$ for a fixed R^*:

$$s = \frac{2(1-R^{*2})R^{*2} \pm \sqrt{E^2(R^{*2}+1)^6 + 4(R^{*2}-1)^2R^{*4}}}{E(R^{*2}+1)^3} \equiv s_\pm. \tag{F7}$$

As $m_2(R^*) \geqslant 0$, $D(s;R^*) \leqslant 0$ holds for $s_- \leqslant s \leqslant s_+$.

Noting that the expression for $\sin(\delta-2\Theta^*)$ in terms of R^* is obtained by solving $d\Theta/dt = 0$, we now show $s_- \leqslant \sin(\delta-2\Theta^*) \leqslant s_+$ for $\Omega' > 0$ as follows. Since Eq. (F7) implies $1 \leqslant s_+$, it is obvious that $\sin(\delta-2\Theta^*) \leqslant s_+$ holds.

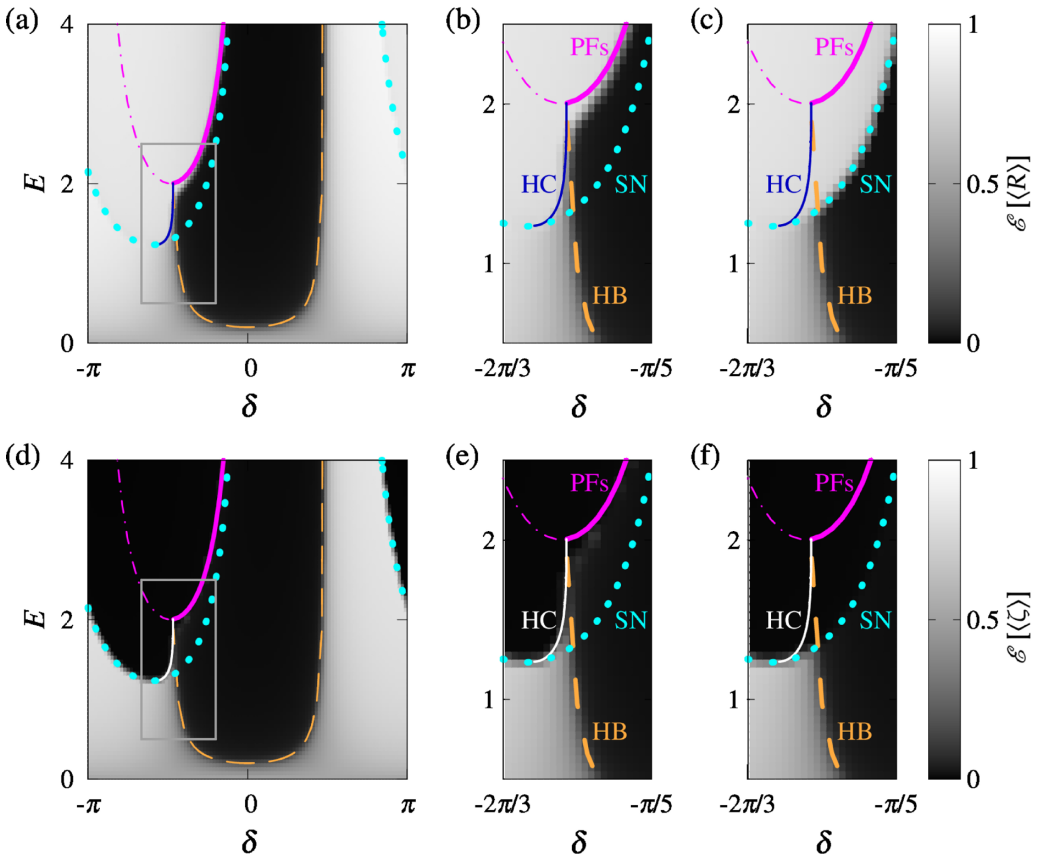

FIG. 10. Simulation results of Eq. (6) with randomized initial conditions and natural frequencies. Mean of the long-time average of (a)–(c) R and (d)–(f) ζ for 10 trials are plotted. The other parameters are the same as those in Fig. 4, and the same bifurcation curves are drawn here. The parameter range in (b), (c), (e), and (f) is the same as that in the boxed area in (a) and (d). The initial phases are drawn from the uniform distribution in (a), (b), (d), and (e) and the Gaussian distribution with mean 0 and standard deviation 0.1 in (c) and (f).

Furthermore,

$$\sin(\delta - 2\Theta^*) - s_- = \sin\delta + \frac{4 + 2K\sin\beta(1+R^{*2})}{E(1+R^{*2})} - \frac{2(1-R^{*2})R^{*2} - \sqrt{E^2(R^{*2}+1)^6 + 4(R^{*2}-1)^2R^{*4}}}{E(R^{*2}+1)^3} \tag{F8}$$

$$\geqslant -1 + \frac{4 + 2K\sin\beta(1+R^{*2})}{E(1+R^{*2})} - \frac{2(1-R^{*2})R^{*2} - E(R^{*2}+1)^3}{E(R^{*2}+1)^3} \tag{F9}$$

$$= \frac{\sigma(R^*)}{E(1+R^{*2})^2}, \tag{F10}$$

where $\sigma(R^*) = 4(1+R^{*2})^2 + 2K\sin\beta(1+R^{*2})^3 - 2(1-R^{*2})R^{*2}$. When $\sin\beta \geqslant 0$, it is obvious that $\Omega' = 1 + K\sin\beta > 0$. In this case, noting $0 \leqslant R^* \leqslant 1$, we obtain $\sigma(R^*) > 0$ because

$$\sigma(R^*) \geqslant 4 + 2K\sin\beta - 2 = 2\Omega'. \tag{F11}$$

We can also show $\sigma(R^*) > 0$ for $\sin\beta < 0$ and $\Omega' > 0$ by calculating the derivative of σ:

$$\frac{d\sigma(R^*)}{dR^*} = 12R^*[1 + 2R^{*2} + K\sin\beta(1+R^{*2})^2]. \tag{F12}$$

The solution of $d\sigma/dR^* = 0$ is given by

$$R^* = \sqrt{\frac{\Omega' + \sqrt{\Omega'}}{-K\sin\beta}} \equiv \tilde{R}^*. \tag{F13}$$

If $\tilde{R}^* > 1$, $\sigma(R^*)$ takes its minimum at $R^* = 1$. Otherwise, the minimum is given by $\min(\sigma(0), \sigma(1))$. Because both $\sigma(0) = 2\Omega' + 2$ and $\sigma(1) = 16\Omega'$ is positive, $\sigma(R^*) > 0$ is satisfied.

Hence, from Eq. (F10), it follows that

$$\sin(\delta - 2\Theta^*) - s_- \geqslant \frac{\sigma(R^*)}{E(1+R^{*2})^2} \geqslant 0. \tag{F14}$$

Therefore, for $\Omega' > 0$, $s_- \leqslant \sin(\delta - 2\Theta^*) \leqslant s_+$ holds, and thus we obtain $|M| = D(\sin(\delta - 2\Theta^*); R^*) \leqslant 0$ for any $R^* \in [0, 1]$.

APPENDIX G: NUMERICAL SEARCH FOR LIMIT-CYCLE SOLUTIONS OF EQ. (8)

While the bifurcation analyses in Sec. III is comprehensive in regard to the local bifurcations, some global bifurcations such as SN bifurcation of periodic orbits are not considered there. These global bifurcations might create or destroy stable limit cycles, affecting the stability region of the synchronously oscillating state in Fig. 1.

Thus, we numerically verified that the stability boundary of the synchronously oscillating state consists of the Hopf, SNIC, and heteroclinic bifurcation curves obtained in Sec. III

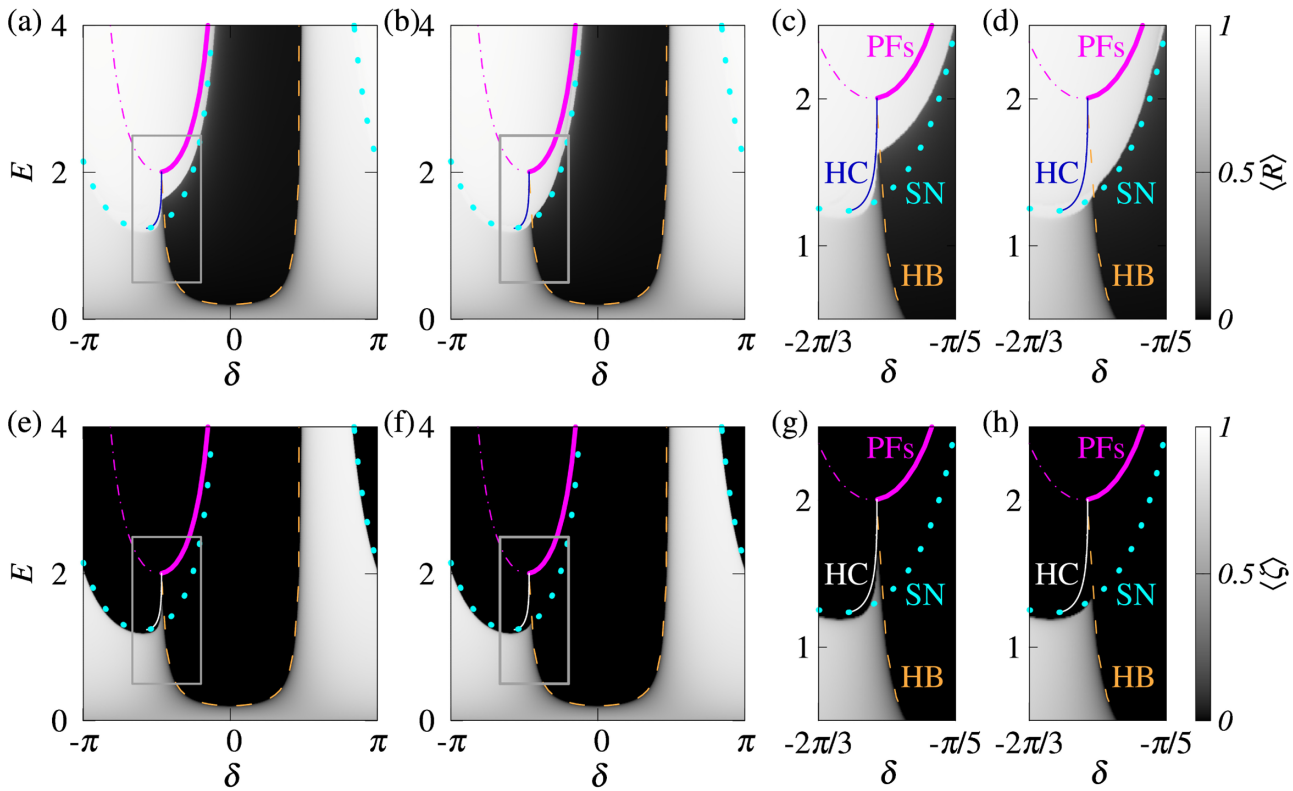

FIG. 11. Simulation results of Eq. (I1). The long-time averages of (a)–(d) R and (e)–(h) ζ for $h = 0.03$ are plotted with the same bifurcation curves as in Fig. 4. The initial condition is $(\mathrm{Re}(r), \mathrm{Im}(r)) = (0.01, 0)$ in (a), (c), (e), and (g) and $(\mathrm{Re}(r), \mathrm{Im}(r)) = (0.9, 0)$ in (b, (d), (f), and (h). The boxed area in (a), (b), (e), and (f) are magnified in (c), (d), (g), and (h), respectively. Parameters are as follows: $K = 0.3$, $\beta = 0$, and $\gamma = 0.1$.

as detailed below. For each parameter set, 100 initial conditions for $\mathrm{Re}(r)$ and $\mathrm{Im}(r)$ are drawn from the uniform distribution on the unit disk, and the type of the attractor to which each orbit converges is detected. In the black region in Fig. 9, at least one orbit converges to a limit cycle. The edge of the black region agrees with the bifurcation curves that are inferred to form the stability boundary of the collective oscillation.

The type of the attractor is classified according to the following criteria. (1) Let Δr_t be the norm of the variation of the orbit between time t and $t+\Delta t$, where $\Delta t = 0.01$. The orbit is considered to be converged to a fixed point if the phase point is moving slowly ($\Delta r_t, \Delta r_{t-\Delta t}, \Delta r_{t-2\Delta t} < 10^{-5}$) and is slowing exponentially ($|\Delta r_t/\Delta r_{t-\Delta t} - \Delta r_{t-\Delta t}/\Delta r_{t-2\Delta t}| < 10^{-5}$). (2) Let $x_{\max}$ and $x_{\min}$ be the maximum and the minimum, respectively, of $\mathrm{Re}(r)$ during an interval ($10\,000 < t < 20\,000$). Then let y_n be the nth intersection of the line $\mathrm{Re}(r) = (x_{\max} + x_{\min})/2$ and the orbit that transverses the line with $\mathrm{Re}(\dot r) > 0$. The orbit is considered to be converged to a limit cycle when $|y_n - y_{n-1}| < 10^{-5}$. With these criteria, we conclude that every orbit is converged to either a fixed point or a limit cycle.

APPENDIX H: NUMERICAL SIMULATION OF EQ. (6) WITH RANDOMELY DRAWN PARAMETERS

In Sec. III we performed numerical simulations of Eq. (6) for $N = 2000$ with natural frequencies $\omega_i = 1 + 0.1\tan[\frac{i\pi}{N} - \frac{(N+1)\pi}{2N}](i = 1, 2, \ldots, N)$ and with two different initial conditions, namely, the uniform state and the fully synchronized state. The simulation result with the former initial condition is expected to represent a typical behavior of the systems with $R \simeq 0$ at $t = 0$, while the latter initial condition is expected to represent the case of $R \simeq 1$ at $t = 0$. However, the complete lack of randomness may make the results obtained in Sec. III atypical.

To confirm that introducing randomness does not qualitatively change the results, we perform the following supplemental numerical simulations and compare the results with Fig. 4. Equation (6) is simulated for 10 times with random initial phases drawn from the uniform distribution on $[0, 2\pi)$ and with natural frequencies drawn from the Lorentz distribution $g(\omega) = \frac{0.1}{\pi}\frac{1}{(\omega-1)^2+0.1^2}$. Then the long-time averages of R and ζ are averaged over these 10 trials to obtain $\mathscr{E}[\langle R\rangle] = \frac{1}{N}\sum_{j=1}^{10}\langle R\rangle^{(j)}$ and $\mathscr{E}[\langle\zeta\rangle] = \frac{1}{N}\sum_{j=1}^{10}\langle\zeta\rangle^{(j)}$, where $\langle R\rangle^{(j)}$ and $\langle\zeta\rangle^{(j)}$ are the value of $\langle R\rangle$ and $\langle\zeta\rangle$ in the jth simulation, respectively. We show $\mathscr{E}[\langle R\rangle]$ in Fig. 10(a) and its magnification Fig. 10(b) and $\mathscr{E}[\langle\zeta\rangle]$ in Fig. 10(d) and its magnification Fig. 10(e). Furthermore, we calculate $\mathscr{E}[\langle R\rangle]$ and $\mathscr{E}[\langle\zeta\rangle]$ for the same system but with initial phases drawn from Gaussian distribution with mean 0 and standard deviation 0.1. In Figs. 10(c) and 10(f), the values of $\mathscr{E}[\langle R\rangle]$ and $\mathscr{E}[\langle\zeta\rangle]$ in this case are plotted for the same parameter region as Figs. 10(b) and 10(e), respectively.

No significant difference between Figs. 4 and 10 can be seen. Although the values of $\mathscr{E}[\zeta]$ in Fig. 10 tend to be slightly larger than those of ζ in Fig. 4, they become comparably small when we performed the simulation for a longer time (results not shown). Therefore, we consider that the numerical results shown in Fig. 4 are robust to the randomness in the natural frequencies and initial conditions.

APPENDIX I: NUMERICAL INVESTIGATION OF THE SYSTEM EXPOSED TO ASYMMETRIC FEEDBACK

Equation (8) is invariant under the change of $r \to -r$. This symmetry is reflected in the types of bifurcation; we obtain the pitchfork and heteroclinic bifurcation curves in Sec. III. As mentioned in Sec. III C and Sec. VI, these bifurcation curves are expected to be replaced with SN and homoclinic bifurcation curves when the oscillators or feedback are modified to break the symmetry.

To investigate how the phase diagrams of the macroscopic state change when the symmetry is broken, we performed numerical simulations for the case where the feedback function includes an asymmetric term. More specifically, we simulated the following equation:

$$\dot r = \left(-\gamma + \frac{Ke^{i\beta}}{2} + i\right)r - \frac{Ke^{-i\beta}}{2}|r|^2 r - \frac{ER[\cos(\Theta - \delta) + h]}{2}(1 - r^2), \tag{I1}$$

where h is a small constant to break the symmetry. Equation (I1) reduces to Eq. (8) for $h = 0$. We show the values of $\langle R\rangle$ for $h = 0.03$ in Figs. 11(a)–11(d) with the bifurcation curves for $h = 0$ that are derived in Sec. III. The initial conditions

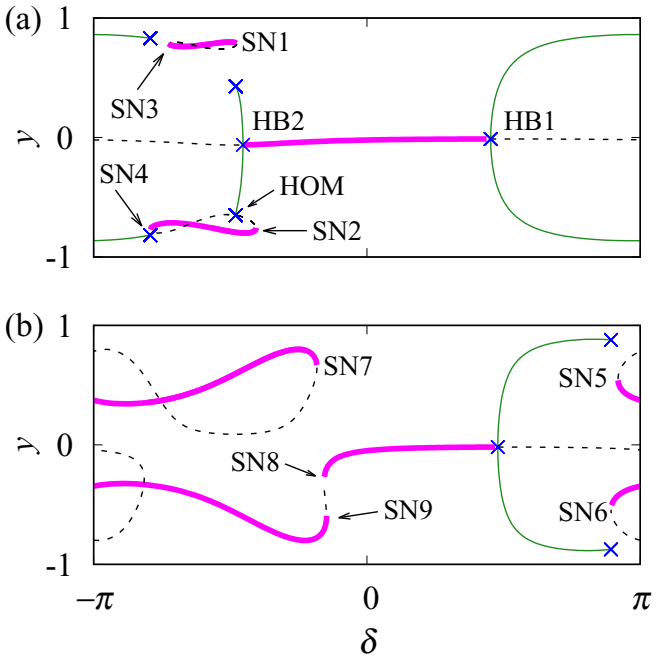

FIG. 12. Bifurcation diagrams of Eq. (I1) for (a) $E = 1.35$ and (b) $E = 3.0$. The horizontal axis is the phase offset of the feedback, and the vertical axis is the imaginary part of the complex order parameter, i.e., $y = \mathrm{Im}(r)$. The points labeled as HB1 and HB2 represent Hopf bifurcation points; the points labeled as SN1, SN2,..., SN9 correspond to SN bifurcation points; and the vector field shown in Fig. 13(a) indicates that a homoclinic bifurcation occurs at the point labeled with HOM. The parameters K, β, γ, and h are the same as in Fig. 11.

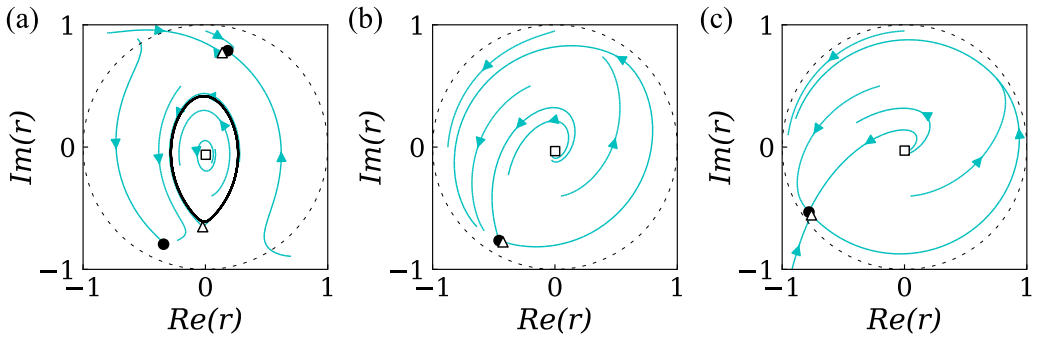

FIG. 13. Vector fields near three of the bifurcation points observed in Fig. 12: (a) HOM point, (b) SN4 point, (c) SN6 point. The vector fields on the complex planes are drawn with cyan arrows. Open squares represent unstable spirals. Filled (resp. open) circles represent stable (resp. unstable) nodes. The open triangles represent saddles. Stable limit cycles are illustrated using black solid curves. The circle drawn with the dashed line on each panel depicts the unit circle on the complex plane.

are as follows: $(\mathrm{Re}(r), \mathrm{Im}(r)) = (0.01, 0)$ in Fig. 11(a) and its magnification Fig. 11(c); and $(\mathrm{Re}(r), \mathrm{Im}(r)) = (0.9, 0)$ in Fig. 11(b) and its magnification Fig. 11(d). Moreover, we plot the values of $\langle \zeta \rangle$ in Figs. 11(e)–11(h). The initial conditions are $(\mathrm{Re}(r), \mathrm{Im}(r)) = (0.01, 0)$ in Figs. 11(e) and 11(g) and $(\mathrm{Re}(r), \mathrm{Im}(r)) = (0.9, 0)$ in Figs. 11(f) and 11(h).

When compared with Fig. 4, which shows the simulation results for the symmetric system, Fig. 11 reveals the similarity in the values of macroscopic variables between systems with and without symmetry. The parameter region where $\langle R \rangle$ is close to 0 in Figs. 11(a), 11(c), and 11(d) are similar to that of Figs. 4(a), 4(b), and 4(c), respectively, although the region where multistability is observed is smaller in Fig. 11. The region where $\langle \zeta \rangle$ is close to 1 in Figs. 11(e), 11(g), and 11(h) are also similar to that of Figs. 4(d), 4(e), and 4(f), respectively.

To further understand how the asymmetry changes the phase diagrams, we choose δ as a bifurcation parameter and numerically obtained bifurcation diagrams for different values of E by using XPPAUT [38]. The obtained diagrams for $E = 1.35$ and $E = 3.0$ are shown in Figs. 12(a) and 12(b), respectively. In these diagrams, the branches of stable and unstable fixed points are represented by thick magenta solid curves and thin black dotted curves, respectively. Green thin solid curves and blue crosses indicate stable and unstable limit cycles, respectively.

Figure 12(a) shows that, as δ is decreased, a limit cycle disappears at the Hopf bifurcation point labeled as HB1, and a stable fixed point appears. When δ is further decreased, another Hopf bifurcation occurs at the point labeled as HB2, and a stable limit cycle appears again. In contrast to the supercriticality proved in Sec. III, these Hopf bifurcations can be subcritical. Actually, unstable limit cycles are detected by XPPAUT in Fig. 12, but only for a small range of δ. In addition, as shown in Fig. 13(a), the vector field near the bifurcation point labeled as HOM indicates that a homoclinic bifurcation occurs at this point. This is in contrast to the heteroclinic bifurcation that is observed in the symmetric system. Another bifurcation that involves fixed points and a stable limit cycle is labeled as SN4. The vector field near this point shown in Fig. 13(b) indicates that a SN bifurcation on an invariant circle occurs.

In Fig. 12(b) a series of SN bifurcation is observed. In particular, SN6 point corresponds to a SN bifurcation on an invariant circle because it occurs at a δ value slightly smaller than that for SN5 and the limit cycle disappears at this δ value. See Fig. 13(c) for the vector field near this point. As seen in Fig. 12(b), the stable fixed point near the origin disappears through the SN bifurcation at SN8, while the transition from the asynchronous state to the oscillation death state occurs through the pitchfork bifurcation in the symmetric system.

[1] A. Pikovsky, M. Rosenblum, and J. Kurths, *Synchronization: A Universal Concept in Nonlinear Sciences* (Cambridge University Press, Cambridge, 2001).

[2] L. Glass, Synchronization and rhythmic processes in physiology, Nature (London) **410**, 277 (2001).

[3] A. Arenas, A. Díaz-Guilera, J. Kurths, Y. Moreno, and C. Zhou, Synchronization in complex networks, Phys. Rep. **469**, 93 (2008).

[4] A. T. Winfree, *The Geometry of Biological Time*, 2nd ed. (Springer, New York, 2001).

[5] Y. Kuramoto, *Chemical Oscillations, Waves, and Turbulence* (Springer, New York, 1984).

[6] A. E. Motter, S. A. Myers, M. Anghel, and T. Nishikawa, Spontaneous synchrony in power-grid networks, Nat. Phys. **9**, 191 (2013).

[7] J. T. Enright, Temporal precision in circadian systems: A reliable neuronal clock from unreliable components? Science **209**, 1542 (1980).

[8] E. D. Herzog, S. J. Aton, R. Numano, Y. Sakaki, and H. Tei, Temporal precision in the mammalian circadian system: A reliable clock from less reliable neurons, J. Biol. Rhythms **19**, 35 (2004).

[9] D. J. Needleman, P. H. E. Tiesinga, and T. J. Sejnowski, Collective enhancement of precision in networks of

coupled oscillators, Physica D: Nonlinear Phenom. **155**, 324 (2001).
[10] H. Kori, Y. Kawamura, and N. Masuda, Structure of cell networks critically determines oscillation regularity, J. Theor. Biol. **297**, 61 (2012).
[11] A. J. Ijspeert, Central pattern generators for locomotion control in animals and robots: A review, Neural Netw. **21**, 642 (2008).
[12] S. Lämmer, H. Kori, K. Peters, and D. Helbing, Decentralised control of material or traffic flows in networks using phase-synchronisation, Physica A: Stat. Mech. Appl. **363**, 39 (2006).
[13] D. R. Aleko and S. Djahel, An IoT enabled traffic light controllers synchronization method for road traffic congestion mitigation, in *Proceedings of 2019 IEEE International Smart Cities Conference* (IEEE, New York, 2019), pp. 709–715.
[14] S. H. Strogatz, D. M. Abrams, A. McRobie, B. Eckhardt, and E. Ott, Crowd synchrony on the Millennium Bridge, Nature (London) **438**, 43 (2005).
[15] C. Hammond, H. Bergman, and P. Brown, Pathological synchronization in Parkinson's disease: Networks, models and treatments, Trends Neurosci. **30**, 357 (2007).
[16] M. M. McGregor and A. B. Nelson, Circuit mechanisms of Parkinson's disease, Neuron **101**, 1042 (2019).
[17] M. J. Armstrong and M. S. Okun, Diagnosis and treatment of Parkinson disease: A review, JAMA **323**, 548 (2020).
[18] P. Limousin and T. Foltynie, Long-term outcomes of deep brain stimulation in Parkinson disease, Nat. Rev. Neurol. **15**, 234 (2019).
[19] J. M. Bronstein, M. Tagliati, R. L. Alterman, A. M. Lozano, J. Volkmann, A. Stefani, F. B. Horak, M. S. Okun, K. D. Foote, P. Krack *et al.*, Deep brain stimulation for Parkinson disease: An expert consensus and review of key issues, Arch. Neurol. **68**, 165 (2011).
[20] M. Kim, M. Bertram, M. Pollmann, A. von Oertzen, A. S. Mikhailov, H. H. Rotermund, and G. Ertl, Controlling chemical turbulence by global delayed feedback: Pattern formation in catalytic CO oxidation on Pt(110), Science **292**, 1357 (2001).
[21] M. Rosenblum and A. Pikovsky, Delayed feedback control of collective synchrony: An approach to suppression of pathological brain rhythms, Phys. Rev. E **70**, 041904 (2004).
[22] M. G. Rosenblum and A. S. Pikovsky, Controlling Synchronization in an Ensemble of Globally Coupled Oscillators, Phys. Rev. Lett. **92**, 114102 (2004).
[23] O. V. Popovych, C. Hauptmann, and P. A. Tass, Effective Desynchronization by Nonlinear Delayed Feedback, Phys. Rev. Lett. **94**, 164102 (2005).
[24] I. Ratas and K. Pyragas, Controlling synchrony in oscillatory networks via an act-and-wait algorithm, Phys. Rev. E **90**, 032914 (2014).
[25] N. Tukhlina, M. Rosenblum, A. Pikovsky, and J. Kurths, Feedback suppression of neural synchrony by vanishing stimulation, Phys. Rev. E **75**, 011918 (2007).
[26] M. Luo, Y. Wu, and J. Peng, Washout filter aided mean field feedback desynchronization in an ensemble of globally coupled neural oscillators, Biol. Cybern. **101**, 241 (2009).
[27] A. Franci, A. Chaillet, E. Panteley, and F. Lamnabhi-Lagarrigue, Desynchronization and inhibition of Kuramoto oscillators by scalar mean-field feedback, Math. Control Signals Syst. **24**, 169 (2012).
[28] O. V. Popovych, B. Lysyansky, M. Rosenblum, A. Pikovsky, and P. A. Tass, Pulsatile desynchronizing delayed feedback for closed-loop deep brain stimulation, PLoS ONE **12**, e0173363 (2017).
[29] S. Zhou, P. Ji, Q. Zhou, J. Feng, J. Kurths, and W. Lin, Adaptive elimination of synchronization in coupled oscillator, New J. Phys. **19**, 083004 (2017).
[30] A. Koseska, E. Volkov, and J. Kurths, Oscillation quenching mechanisms: Amplitude vs. oscillation death, Phys. Rep. **531**, 173 (2013).
[31] E. Ott and T. M. Antonsen, Low dimensional behavior of large systems of globally coupled oscillators, Chaos **18**, 037113 (2008).
[32] E. Ott and T. M. Antonsen, Long time evolution of phase oscillator systems, Chaos **19**, 023117 (2009).
[33] P. Ashwin, S. Coombes, and R. Nicks, Mathematical frameworks for oscillatory network dynamics in neuroscience, J. Math. Neurosci. **6**, 2 (2016).
[34] T. Stankovski, T. Pereira, P. V. E. McClintock, and A. Stefanovska, Coupling functions: Universal insights into dynamical interaction mechanisms, Rev. Mod. Phys. **89**, 045001 (2017).
[35] H. Sakaguchi and Y. Kuramoto, A soluble active rotater model showing phase transitions via mutual entertainment, Prog. Theor. Phys. **76**, 576 (1986).
[36] K. H. Nagai and H. Kori, Noise-induced synchronization of a large population of globally coupled nonidentical oscillators, Phys. Rev. E **81**, 065202 (2010).
[37] J. Guckenheimer and P. Holmes, *Nonlinear Oscillations, Dynamical Systems, and Bifurcations of Vector Fields* (Springer-Verlag, 1983).
[38] B. Ermentrout, *Simulating, Analyzing, and Animating Dynamical Systems: A Guide to XPPAUT for Researchers and Students* (SIAM, 2002).
[39] L. M. Childs and S. H. Strogatz, Stability diagram for the forced Kuramoto model, Chaos **18**, 043128 (2008).
[40] H. Daido, Scaling behaviour at the onset of mutual entrainment in a population of interacting oscillators, J. Phys. A: Math. Gen. **20**, L629 (1987).
[41] S. H. Strogatz, *Nonlinear Dynamics and Chaos*, 2nd ed. (Westview Press, Boulder, 2014).
[42] J. T. Ariaratnam and S. H. Strogatz, Phase Diagram for the Winfree Model of Coupled Nonlinear Oscillators, Phys. Rev. Lett. **86**, 4278 (2001).
[43] D. S. Goldobin and A. Pikovsky, Effects of delayed feedback on Kuramoto transition, Prog. Theor. Phys. Suppl. **161**, 43 (2006).
[44] O. V. Popovych, C. Hauptmann, and P. A. Tass, Control of neuronal synchrony by nonlinear delayed feedback, Biol. Cybern. **95**, 69 (2006).
[45] O. V. Popovych and P. A. Tass, Multisite delayed feedback for electrical brain stimulation, Frontiers in Physiology **9**, 46 (2018).
[46] X. Zhang and S. Liu, Nonlinear delayed feedback control of synchronization in an excitatory-inhibitory coupled neuronal network, Nonlinear Dyn. **96**, 2509 (2019).
[47] O. V. Popovych, C. Hauptmann, and P. A. Tass, Impact of nonlinear delayed feedback on synchronized oscillators, J. Biol. Phys. **34**, 267 (2008).

[48] I. Z. Kiss, C. G. Rusin, H. Kori, and J. L Hudson, Engineering complex dynamical structures: Sequential patterns and desynchronization, Science **316**, 1886 (2007).

[49] H. Kori, C. G. Rusin, I. Z. Kiss, and J. L. Hudson, Synchronization engineering: Theoretical framework and application to dynamical clustering, Chaos **18**, 026111 (2008).

[50] D. R. Merrill, M. Bikson, and J. G. R. Jefferys, Electrical stimulation of excitable tissue: Design of efficacious and safe protocols, J. Neurosci. Methods **141**, 171 (2005).

[51] I. Z. Kiss, Y. Zhai, and J. L. Hudson, Predicting Mutual Entrainment of Oscillators with Experiment-Based Phase Models, Phys. Rev. Lett. **94**, 248301 (2005).

[52] H. Kori, Y. Kuramoto, S. Jain, I. Z. Kiss, and J. L. Hudson, Clustering in globally coupled oscillators near a Hopf bifurcation: Theory and experiments, Phys. Rev. E **89**, 062906 (2014).

[53] D. Iatsenko, P. V. E. McClintock, and A. Stefanovska, Extraction of instantaneous frequencies from ridges in time-frequency representations of signals, Signal Proc. **125**, 290 (2016).

[54] Y. Kobayashi and H. Kori, Design principle of multi-cluster and desynchronized states in oscillatory media via nonlinear global feedback, New J. Phys. **11**, 033018 (2009).

[55] A. T. Winfree, Biological rhythms and the behavior of populations of coupled oscillators, J. Theor. Biol. **16**, 15 (1967).